Journal of Controlled Release 390 (2026) 114539

Contents lists available at ScienceDirect

Journal of Controlled Release

journal homepage: www.elsevier.com/locate/jconrel

Understanding excipient interactions unlocks untapped potential of RNA-lipid nanoparticles in dry powder formulations for local pulmonary delivery☆

Nora Martini [a], Leonie Deßloch [a,b], Taras Sych [c], Otto Berninghausen [d], J. Merl-Pham [e], Sjoerd Dijkstra [a], Simone P. Carneiro [a,f,g], Marion Frankenberger [h], Roland Beckmann [d], Jürgen Behr [i], Gabriele Matschiner [b], Christine Schuberth-Wagner [b], A. Önder Yildirim [h,j], David C. Jürgens [a,b,f], Erdinc Sezgin [c], Olivia M. Merkel [a,b,f], Benjamin Winkeljann [a,b,f,g,*]

[a] Department of Pharmacy, Comprehensive Pneumology Center (CPC-M), Ludwig-Maximilians-Universität München, Member of the German Center for Lung Research (DZL), 81377 Munich, Germany
[b] RNhale GmbH, Am Klopferspitz 19, 82152 Planegg, Germany
[c] Science for Life Laboratory, Department of Women's and Children's Health, Karolinska Institutet, Solna, Sweden
[d] Gene Center and Department of Biochemistry, University of Munich, Munich 81377, Germany
[e] Metabolomics and Proteomics Core, Helmholtz Zentrum Munich, Ingolstaedter Landstr. 1, 85764 Neuherberg, Germany
[f] Center for NanoScience (CeNS), Ludwig-Maximilians-Universität München, Munich, Germany
[g] Pharmaceutical Engineering and Technology Research Scientists (PETRS), Germany
[h] Institute of Lung Health and Immunity (LHI) with CPC-M bioArchive, Comprehensive Pneumology Center (CPC-M), Helmholtz Munich, Member of the German Center for Lung Research (DZL), Munich, Germany
[i] Department of Medicine V, LMU University Hospital, Comprehensive Pneumology Center (CPC-M), Ludwig-Maximilians-Universität München, Member of the German Center for Lung Research (DZL), Munich, Germany
[j] Institute of Experimental Pneumology, Ludwig-Maximilians University (LMU), Munich, Germany

ARTICLE INFO

Keywords:
Lung delivery
Spray drying
Molecular dynamic simulation
Lipid nanoparticles
Mucus diffusion

ABSTRACT

Small interfering RNA (siRNA)-loaded lipid nanoparticles (LNPs) are a promising modality for gene silencing therapies. Pulmonary delivery offers an attractive, non-invasive route to target respiratory diseases. However, the development of stable dry powder formulations suitable for inhalation remains a key challenge. In this study, we investigated the impact of spray drying on the physicochemical integrity and biological performance of siRNA-LNPs. Four LNP formulations differing in PEG-lipid helper lipid content were subjected to spray drying in the presence of a lactose matrix. The impact of formulation parameters on physicochemical integrity, colloidal stability, structural preservation, and biological behaviour was systematically evaluated before and after spray drying and predicted by molecular dynamic simulations. Choosing this holistic approach demonstrates that LNP composition critically influences suitability for spray drying and provides key insights for the development of stable pulmonary siRNA therapies.

1. Introduction

The coming of age of RNA-based vaccines during the pandemic is estimated to have saved >14 M lives [1], and novel RNA-based drugs are being developed for indications ranging from Alzheimer's disease to cancers. A major challenge in developing these therapies is the need for targeted delivery, as off-target effects in non-target organs pose substantial risks. Local administration directly to target tissues can mitigate many toxicological issues associated with systemic delivery. While RNA therapeutics are theoretically well-suited for treating pulmonary disorders via localized lung administration, this route presents significant challenges in practice. To address these difficulties, dry powder

☆ This article is part of a Special issue entitled: 'Young Investigator Issue' published in Journal of Controlled Release.

* Corresponding author at: Department of Pharmacy, Comprehensive Pneumology Center (CPC-M), Ludwig-Maximilians-Universität München, Member of the German Center for Lung Research (DZL), 81377 Munich, Germany.
E-mail address: benjamin.winkeljann@cup.lmu.de (B. Winkeljann).

https://doi.org/10.1016/j.jconrel.2025.114539
Received 31 July 2025; Received in revised form 20 November 2025; Accepted 11 December 2025
Available online 12 December 2025

formulations of RNA-loaded lipid nanoparticles (RNA-LNPs) have been proposed. These formulations can be delivered to the lungs using well-established dry powder inhalers, which offer a rapid, non-invasive method, and are associated with favorable storage stability.

However, conversion of LNPs into dry powder formulations remains technically challenging, and the underlying physical mechanisms are still incompletely understood. Spray drying (SD) and lyophilization (freeze-drying) are the two primary methods employed to generate dry RNA-LNP powders, with each introducing distinct stress factors that must be carefully controlled [2]. SD, in particular, imposes shear stress during pumping and during atomization of the liquid feed, and thermal stress during droplet drying. While the high inlet temperature of the drying gas may initially seem problematic, the evaporative cooling effect ensures that the internal droplet temperature remains relatively low during atomization and the early drying phase. However, as particles travel through the drying chamber and residual moisture decreases, the exposure to elevated outlet temperatures increases, which can potentially lead to lipid phase transitions, membrane fusion, or RNA degradation.

Empirical evidence underscores these concerns. Several studies have reported structural changes in RNA-LNPs following SD, most notably an increase in particle size upon rehydration. Zimmermann et al. reported SD siRNA-LNPs maintained in vitro efficacy after drying at an inlet temperature of 100 °C [3]. Nevertheless, dynamic light scattering (DLS) measurements revealed a significant increase in the hydrodynamic diameter of the LNPs after reconstitution, suggesting structural rearrangement. Similarly, Friis et al. formulated SD mRNA-LNPs for intratracheal delivery. Post-drying characterization revealed an increased proportion of particles exceeding 200 nm in diameter, as well as the formation of electron-dense lining around the LNP observed via cryo-TEM [4]. Interestingly, Gordon et al. found that spray-freeze drying, a technique which does not induce thermal stress, also led to size increases of LNPs after redispersion, pinpointing that drying-induced reorganization is not solely thermally driven [5].

To protect lipid membranes during drying, the incorporation of sugars, which are known to provide lyo- and cryoprotective effects on biomembranes, is a widely adopted strategy. Two principal models have been proposed to explain their protective mechanisms: the preferential exclusion model and the preferential interaction model. The preferential exclusion model describes that the sugars are excluded from the immediate vicinity of the membrane and thereby preserve a hydration shell that stabilizes the lipid bilayer [6–11]. The preferential direct interaction model, in contrast, encompasses three, not mutually exclusive, hypotheses: (i) water replacement, in which sugars substitute for water molecules through hydrogen bonding with lipid headgroups; (ii) entrapment, where sugars immobilize residual water, reducing ice crystallization; and (iii) vitrification, whereby the formation of a glassy sugar matrix physically stabilizes membrane structures during drying or freezing [12–19].

In addition to the technological challenges of drying RNA-LNPs, several biological barriers must be overcome for efficient pulmonary delivery. The LNPs must traverse the mucus layer in the upper airways or the lung lining fluid in the alveoli, with factors like mucus clearance and turnover time being crucial. Upon reaching the target tissue, the LNPs must cross the extracellular matrix for cellular uptake. For LNPs, cellular internalization is significantly influenced by the proteins adsorbed onto their surface, forming a protein corona after administration. This phenomenon has been utilized in early LNP formulations to promote an apolipoprotein (ApoE)-rich corona, enhancing uptake by hepatocytes through the low-density lipoprotein receptor (LDL-R). In pulmonary delivery, LNPs are exposed to different proteins, and the effects of these interactions on LNP behaviour in the lungs remain mostly unclear.

Here, we dissect the mechanisms underlying the performance of dry powder-formulated LNPs for pulmonary RNA delivery. We systematically characterize SD-induced structural changes using an orthogonal set of advanced methodologies, including molecular dynamics simulations, cryo-TEM, and membrane fluidity measurements. We show that the concentration of PEG-lipid and the choice of helper lipid critically modulate interactions between excipients and the LNP membrane, promoting hydrogen bonding and partial excipient incorporation that drive morphological alterations. Even after reconstitution, membranes remain in a less fluid state, with PEG and helper lipid content dictating the extent of this effect. These structural changes influence LNP diffusion through mucus, cellular uptake, and RNA silencing efficiency. Using in situ diffusion assays, fluorescence correlation spectroscopy, and air–liquid interface (ALI) cell models, we further demonstrate formulation-specific differences in LNP transport across lung barriers and intracellular delivery. Finally, we characterize the composition of the protein corona that forms on LNPs upon contact with human bronchoalveolar lavage fluid, offering what is, to our knowledge, the first reported analysis of its kind.

2. Materials and methods

2.1. Materials

(6Z,9Z,28Z,31Z)-heptatriaconta-6,9,23,31-tetraen-19-yl 4-(dimethylamino)butanoate (D-Lin-MC3-DMA) was obtained from MedChemExpress (Monmouth Junction, USA) and Corden Pharma (Plankstadt, Germany). 1,2-distearoyl-sn-glycero-3-phosphocholine (DSPC), 3β-hydroxy-5-cholesten (cholesterol), and 1,2-dimyristoyl-rac-glycero-3-methoxypolyethylene glycol-2000 (PEG-DMG 2000), as well as absolute ethanol, highly purified water (HPW), 6-dodecanyl-2-dimethylaminonaphthalene (Laurdan), TNS reagent (6-(p-toluidino-2-naphthalenesulfonic acid sodium salt)), and dimethyl sulfoxide (DMSO), sodium phosphate, sodium borate, sodium citrate, sodium hydroxide, and EDTA (2 mM), foetal bovine serum (FBS), penicillin-streptomycin (1 %), G418 (0.4 %), RPMI 1640 media, and EMEM media, sterile egg yolk emulsion, mucin (bovine submaxillary gland), Atto 647 N DOPE, calf thymus DNA (Type I), DTPA solution (1 mg/ml), sodium chloride, sucrose and potassium chloride were purchased from Sigma-Aldrich (Taufkirchen, Germany). eGFP siRNA and siNC were obtained from Integrated DNA Technologies (IDT, Leuven, Belgium) and Sigma-Aldrich (Taufkirchen, Germany). RiboGreen® RNA quantification reagent and TE buffer, phosphate buffered saline (PBS), LysoTracker™ Red DND-99, Alexa Fluor 647, and 4′,6-diamidino-2-phenylindole (DAPI) were obtained from Thermo Fisher Scientific (Darmstadt, Germany). Lactose monohydrate (Inhalac® 230) was purchased from Meggle (Wasserburg, Germany). The human non-small lung carcinoma cell line H1299 stably expressing enhanced green fluorescent protein (H1299-eGFP) was purchased from ATCC (VA, USA), and Calu-3 cells were sourced from LGC Standards (Wesel, Germany). PneumaCult™ ALI medium was sourced from STEMcell Technologies (Vancouver, Canada). Rhodamine-labelled lipid 18:1 Liss Rhod PE was purchased from Avanti Research (Birmingham, AL, USA). Plastics and consumables, including Vivaspin 500 columns (10,000 MWCO PES), Vivaspin 6 columns (30,000 MWCO PES), 384-well plates, 96-well black flat-bottom plates, 24-well plates, Transwell plates (24-well, 6.5 mm, PET, 8 μm pores), and Corning Transwell inserts (6.5 mm, 0.4 μm), were purchased from VWR (Darmstadt, Germany) and Greiner (Frickenhausen, Germany). 3.5 kDA, Pur-A-Lyzer TM Mega Dialysis kit was purchased from Sigma-Aldrich (Taufkirchen, Germany). 8-well μ-slides were obtained from ibidi GmbH (Martinsried, Germany). 0.22 μm Acrodisc® syringe filters were obtained from Pall (Dreieich, Germany) and disposable DLS cuvettes from Brand GmbH & Co. KG (Wertheim, Germany).

2.2. Preparation of siRNA LNPs

Small interfering RNA-loaded LNPs were formulated based on the Onpattro® formulation, with variations in helper lipid and PEG-lipid content (Table 1). Lipids were dissolved in absolute ethanol at a

Table 1
Percentages of different lipids in the four LNP compositions.

	LNP 1	LNP 2	LNP 3	LNP 4
D-Lin-MC3-DMA	50 %	50 %	50 %	50 %
Cholesterol	39.5 %	24.5 %	38.5 %	23.5 %
DSPC	10 %	25 %	10 %	25 %
PEG-DMG 2000	0.5 %	0.5 %	1.5 %	1.5 %

concentration of 5 mM and mixed according to the specified ratios (Table 1). siRNA was diluted in 25 mM sodium acetate buffer (pH 4) to achieve an N/P ratio of 3. The lipid and siRNA solutions were mixed using either impingement jet mixing (KNAUER Nanoscaler®, KNAUER, Berlin, Germany) at a total flow rate (TFR) of 3 ml/min, or syringe pumps (Landgraf L100, Landgraf Laborsysteme HLL GmbH, Langenhagen, Germany) connected to a T-junction mixer (Techlab, Braunschweig, Germany) at a TFR of 2 ml/min to produce precursor LNPs. For both mixing methods, a lipid-to-siRNA flow rate ratio (FRR) of 1:3 was used. Precursor LNPs were dialyzed overnight at room temperature against PBS (pH 7.4) using a 3.5 kDa MWCO dialysis kit, then sterile filtered using a 0.22 μm syringe filter. Final LNPs were stored at 4 °C for up to 30 days until further use.

2.3. Spray-drying of siRNA LNPs

Feed solutions were prepared by adding lactose monohydrate to LNP suspensions to reach a solid content of 50 mg/ml. This lactose-LNP solution was spray-dried following the method by Friis et al. [4] SD was performed using a Mini Spray Dryer B-290 (Büchi Labortechnik, Flawil, Switzerland) with the following adjusted parameters: inlet temperature 100 °C, outlet temperature ~ 64 °C, pump rate 10 %, atomizing gas flow 473 L/h, and aspirator set to 80 %. The powder was collected using a high-performance cyclone. Two siRNA concentrations were processed, resulting in final concentrations of 40 and 16 pmol siRNA/mg lactose (corresponding to 0.67 μg/mg and 0.27 μg/mg, respectively).

2.4. Hydrodynamic diameters and zeta potential

Hydrodynamic diameter and polydispersity index (PDI) were measured by dynamic light scattering (DLS) using a Zetasizer Advance Ultra (Malvern Instruments, Malvern, UK) at 25 °C in disposable cuvettes. SD powders were redispersed in purified water to obtain a lactose concentration of 50 mg/ml and diluted 1:5 in PBS or measured directly. Measurements were performed in triplicate ($n = 3$), and data were analyzed using ZS Xplorer software (v 3.1.5.1). Results are reported as *Z*-average (nm) ± SD. Nanoparticle tracking analysis (NTA) was performed using the NanoSight NS300 system (Malvern Instruments, Malvern, UK). Samples were diluted to achieve 10–200 particles per frame and measured at 25 °C. Five runs per sample were conducted.

2.5. Laurdan assay

LNPs were stained with Laurdan at a lipid-to-Laurdan molar ratio of 100:1 in a 1 mg/ml Laurdan ethanol solution. Non- SD LNPs were diluted 1:2 with HPW, LNPs were also supplemented with a lactose solution (50 mg/ml) and SD LNPs were reconstituted to 50 mg/ml lactose in HPW and incubated for 30 min resulting in the same lipid concentrations in all solutions. Samples (100 μl) were transferred to a 96-well plate and fluorescence was measured in triplicates using a Spark® microplate reader. Excitation was at 340 nm, and emission was measured at 490 nm and 440 nm. Laurdan general polarization (Gp) was calculated using the formula introduced by Parasassi et al [20]:

$$Gp = \frac{(I_{440nm} - I_{490nm})}{(I_{440nm} + I_{490nm})}$$

2.6. Molecular dynamics simulations

All molecular dynamics (MD) simulations were performed using GROMACS 2021.4 patched with PLUMED [21–23]. All-atom (AA) membrane systems were constructed with the CHARMM-GUI Multicomponent Assembler [24,25]. Lactose, built using the CHARMM-GUI Glycan Reader, was positioned in close proximity to the membrane within the simulation box. The Multicomponent Assembler utilizes CHARMM GUIs Membrane builder [26,27] which was extended in 2021 to support ionizable lipids relevant for LNP systems [28].

Membrane components were selected to align with the Onpattro® LNP formulation, though different concentrations of unprotonated D-Lin-MC3-DMA were used to better mimic the membrane composition of a nucleic acid-loaded LNP. The concentrations of other membrane lipids were adjusted as shown in Supplementary Table 1. The simulation box was 7 nm × 7 nm × 17 nm, with the extended z-dimension accommodating PEG-DMG 2000 molecules.

For hydrated and rehydrated simulations, the dehydrated membrane system was hydrated using the TIP3P water model, as recommended by GROMACS. The system was neutralized and isotonised with sodium and chloride ions following CHARMM-GUI guidelines. Simulations were run using the GROMACS-compatible Charmm36 force field [29]. Energy minimization for hydrated and rehydrated systems was conducted in a stepwise manner for 50,000 steps. Coulombic interactions were treated using Particle Mesh Ewald (PME) electrostatics with a cutoff distance of 1.2 nm. Van der Waals interactions were handled using a cutoff algorithm with the same 1.2 nm cutoff. Equations of motion were integrated using the leap-frog algorithm during equilibration and production runs. The system underwent a 0.125 ns NVT equilibration at 303.15 K (v-rescale thermostat), maintaining constant number of atoms and volume. This was followed by a 0.125 ns NPT equilibration using position restraints at 1 atm pressure (Berendsen barostat) and 303.15 K temperature (v-rescale thermostat). Production simulations were conducted for 10 ns under constant temperature (303.15 K, Nose–Hoover thermostat) and semi-isotropic pressure (1 atm, Parrinello–Rahman barostat).

For dehydrated systems, due to pressure instabilities in low-solvation conditions, energy minimization and NVT equilibration were performed as described above. The production run was conducted under NVT conditions with temperature coupling via the Nose–Hoover thermostat at 303.15 K.

Analysis included solvent-accessible surface area (SASA), number of hydrogen bonds, mean square displacement (MSD) of lactose, radial distribution function (RDF) of lactose relative to membrane components, symmetrized mass density, and area per lipid (for NPT simulations). SASA and hydrogen bond analysis was performed from 1 ns to 10 ns.

2.7. Determination of apparent pKa

A master buffer stock was prepared by mixing 10 mM sodium phosphate, 10 mM sodium borate, 10 mM sodium citrate, and 150 mM sodium chloride as described by Sabnis et al. [30] The pH was adjusted to values from 3 to 9 with sodium hydroxide, resulting in 14 pH conditions. TNS reagent (20.75 mM in DMSO) was added to the LNPs, which were concentrated to 500 μM lipid using a Vivaspin 500 column at 3000 g. For non- SD LNPs, 90 μl of each pH buffer was added into a 96-well plate. For SD LNPs, the pH range was adjusted from 3 to 8. 5 μl of LNP sample and 5 μl of TNS reagent (84 μM) were added to each well, incubated for 20 min at RT, and measured using a Spark® microplate reader at 320 nm excitation and 450 nm emission. The pKa was determined using a four-parameter logistic regression fit, with the value where 50 % of fluorescence intensity was measured.

2.8. Cryo-TEM

For Cryo-TEM imaging fresh or SD LNPs were concentrated using

Vivaspin 6 columns at 3500 G for up to 3 h, until reaching a siRNA concentration of 1000 ng/μl. Afterwards the samples were stored at 4 °C overnight. For imaging 3.5 μl of each sample was applied to 2 nm carbon-coated Quantifoil R3/3 holey copper-supported grids and vitrified using a Vitrobot Mark IV (FEI/Thermo Fisher). Micrographs of the vitrified samples were collected under low dose conditions at various nominal magnifications using EM- TOOLS (TVIPS GmbH) on a Tecnai G2 Spirit transmission electron microscope (FEI/Thermo Fisher), equipped with a F218 2048 × 2048 pixel CCD camera (TVIPS GmbH) operating at 120 kV.

2.9. In vitro uptake and eGFP knockdown kinetics in H1299-eGFP cells

H1299-eGFP cells were cultured in RPMI 1640 media supplemented with 10 % foetal bovine serum (FBS), 1 % penicillin-streptomycin and 0.4 % G418. Cells were maintained, grown and incubated in a humidified incubator at 37 °C and 5 % CO2. 30,000 cells were seeded in 24-well plates and incubated for 24 h before transfection. LNPs containing eGFP-siRNA labelled with Alexa-Fluor 647 were diluted in sterile PBS (fresh LNPs) or reconstituted in RNase-free water (SD LNPs) to a final siRNA concentration of 800 pmol/ml and 100 μl added to each well. Blank samples were treated with 100 μl PBS. At 0.5, 1, 2, 4, 8, 16, and 24 h post transfection, the medium was removed, and cells were washed with PBS and trypsinised. The reaction was stopped by adding 200 μl of growth medium. The cell suspension was collected and centrifuged at 400 *g* for 5 min. Afterwards, supernatant was aspirated, cells washed with PBS, centrifuged, and finally suspended in 400 μl PBS with 2 mM EDTA. Cellular uptake and eGFP knockdown were measured using flow cytometry (Attune NxT, Thermo Fisher Scientific, Waltham, MA, USA), with excitation at 638 nm and 488 nm, detected with RL-1H and BL-1H filters. Data were collected from 10,000 viable gated cells per sample. Cellular uptake is reported as mean fluorescence intensity (MFI), while knockdown efficiency is expressed as % eGFP expression relative to blank controls. The knockdown half-time was derived by fitting the eGFP expression data to a four-parameter logistic regression model, with the time point corresponding to 50 % maximal expression defined as T1/2.

2.10. Confocal microscopy

H1299-eGFP cells (10,000 cells) were seeded in 8-well μ-slides and incubated for 24 h at 37 °C with 5 % CO_2. One hour prior to transfection, the medium was aspirated, cells washed with PBS and stained with 50 nM LysoTracker Red DND-99 in growth medium. Fresh LNPs were diluted in sterile PBS, SD LNPs were reconstituted in sterile RNase-free water to a siRNA concentration of 800 pmol/ml and 40 μl added to each well. Blank samples were treated with 40 μl PBS. After 4 h, the medium was removed, and cells were washed with PBS. For nuclei staining, cells were incubated with 0.5 μg/ml DAPI in PBS for 15 min in absence of light, followed by 3× PBS washes. Live-cell imaging was performed using a Leica TCS SP8 inverted confocal laser scanning microscope (DMI8-CS platform) equipped with a HC PL APO CS2 40×/1.30 NA oil immersion objective. Excitation was performed using diode or OPSL lasers at 405 nm (DAPI), 488 nm (lysotracker), and 638 nm (AF647), with detection windows set to 410–490 nm (blue, PMT), 493–643 nm (green, PMT), and 643–776 nm (red, HyD), respectively. Image acquisition was carried out sequentially across frames to minimize spectral overlap. Images were collected under identical acquisition settings across conditions and processed using Leica Application Suite X software (LAS X, Leica Microsystems, Wetzlar, Germany).

2.11. Preparation and characterization of artificial mucus

Artificial mucus following a protocol published by Conte et al. [31] with slight modifications. In brief, a mixture containing 25 μl of sterile egg yolk emulsion, 25 mg of mucin from bovine submaxillary glands, 20 mg of calf thymus DNA (Type I), 30 μl of an aqueous DTPA solution (1 mg/ml), 25 mg of sodium chloride, 11 mg of potassium chloride, 100 μl of RPMI 1640 medium, 50 μl of penicillin-streptomycin, and RNase-free water to obtain a total volume of 5 ml was prepared. The mixture was vortexed, stirred for 1 h, and degassed for 4 h in a vacuum oven at 20 °C. The mucus was allowed to rest at 4 °C overnight. Rheological characterization was performed using a Physica MCR 100 rheometer (Anton Paar, Graz, Austria) equipped with a cone-plate geometry (CP50–1, Anton Paar). Viscosities were measured across shear rates ranging from $d\gamma/dt = 1000\ s^{-1}$ to $d\gamma/dt = 10\ s^{-1}$. A strain-controlled frequency sweep from f = 0.10 Hz to f = 10 Hz was conducted to assess frequency-dependent viscoelasticity. Eleven equidistant data points were recorded on a logarithmic scale at 20 °C. A solvent trap was used to prevent sample dehydration during measurements.

2.12. Fluorescence correlation spectroscopy

Diffusion coefficient of LNPs in PBS and mucus was measured using Fluorescence Correlation Spectroscopy (FCS). LNPs were labelled using Atto 647 N DOPE. LNPs (20 μl) were mixed with 1 μl of 1 mg/ml Atto 647 N DOPE solution in DMSO. Furthermore, 10 μl of labelled LNPs were added to 100 μl of PBS or 100 μl of mucus. A Zeiss LSM 980 microscope with 40 × 1.2NA water immersion objective was used for FCS. A 633 nm He—Ne laser was used for excitation. The laser power was set to 0.05 % of the total laser power, corresponding to 1 μW. The emission detection was done with GaAsP spectral detector in the range of 650–700 nm. FCS fitting and diffusion coefficient calculation was performed using the home-made python based program Py-Profiler [32]. Curves were fitted with the following three-dimensional diffusion model:

$$G(\tau) = \frac{1}{\langle N \rangle}\left(1 + \frac{\tau}{\tau_D}\right)^{-1}\left(1 + \frac{\tau}{AR^2\tau_D}\right)^{\frac{1}{2}}$$

where $G(\tau)$ is a correlation function, τ stands for delay time, τ_D – for diffusion time, AR – for aspect ratio of the focal volume and $\langle N \rangle$ - for an average number of molecules within the focal volume. Calibration was performed using 10 nM solution of Alexa Fluor 647 in pure water. Diffusion was calculated from the diffusion time using the following expression:

$$D = \frac{\omega^2}{8ln2\tau_D}$$

where D is a diffusion coefficient, ω stands for full width at half maximum of focus point spread function, τ_D for diffusion time.

2.13. In vitro penetration through artificial mucus

LNP formulations for the mucus penetration assay were prepared with 2 mol% Rhodamine-labelled DOPE. A volume of 50 μl artificial mucus was transferred to the insert of a 24-well Transwell system, and 20 μl of either fresh or reconstituted SD LNPs was added on top. The acceptor compartment contained 500 μl PBS. The plate was incubated at 37 °C in a humidified incubator. At 0.5, 1, 2, 4, 8, and 24 h, 100 μl of the acceptor medium was collected for analysis and replaced with fresh PBS. Diffusion control wells contained 50 μl PBS instead of mucus and were processed identically. Fluorescence intensity was measured using a Tecan Spark® microplate reader with excitation at 540 nm and emission at 590 nm. Results are presented as cumulative LNP penetration through mucus relative to the diffusion control.

2.14. Mucus penetration and transfection efficiency in mucus-secreting Calu-3 cells grown at the air liquid interface (ALI)

Calu-3 cells were cultured in EMEM medium supplemented with 10 % FBS and maintained in a humidified incubator at 37 °C and 5 % CO_2. A

total of 250,000 cells were seeded onto Corning Transwell inserts and placed into wells containing 700 µl culture medium at the basolateral side. After three days, a dense monolayer had formed. For air–liquid interface culture, the apical medium was removed, and the basolateral medium was exchanged for 200 µl PneumaCult ALI medium, refreshed every two days. After six days, a stable polarized epithelial layer had formed. The diffuse mucus layer was washed with 200 µl PBS, and 24 h later, cells were transfected with 100 µl fresh or reconstituted Alexa-Fluor 647-labelled siRNA-LNPs at 1.6 nmol/ml siRNA. Blank samples were treated with 100 µl PBS. After 6 h of incubation at 37 °C and 5 % CO_2, cells were gently scraped off the Transwell membrane, suspended in PBS, and centrifuged at 400 *g* for 5 min. The supernatant was removed, cells were washed with PBS, centrifuged again, and resuspended in 400 µl PBS containing 2 mM EDTA. Flow cytometry (Attune NxT) was used to measure cellular uptake with a 638 nm excitation laser and RL-1H filter detection. The experiment was performed once in triplicates. Results are presented as mean ± s.d. of transfected cells (%) relative to blank samples.

2.15. Sampling of human bronchoalveolar lavage fluid (BALF)

Human bronchoalveolar lavage (BAL) fluid samples from post-lung transplantation (post-LTx) patients were obtained from the CPC-M bioArchive at the Comprehensive Pneumology Center (CPC Munich, Germany).

Bronchoalveolar lavage was performed as described previously [33]. In brief, after the upper airways and trachea are anesthetized with a xylocaine-spray, a standard fiberoptic bronchoscope is inserted through the nose or mouth into the tracheobronchial tree. Following routine evaluation of the respiratory tract, the tip of the bronchoscope is wedged into a subsegmental bronchus of the lingula or right middle lobe. Once the bronchoscope is wedged 20 ml of 0.9 % sterile saline is inserted in the suction port by the use of a syringe. The fluid is immediately pulled back and the fluid is collected in a 50-ml plastic tube. This process of lavage and suction is then repeated five times (total fluid, 100 ml). In general, 40–60 % of the infused volume is recovered. BAL fluid was obtained in frozen form from the CPC-M bioArchive and stored at −80 °C until analyzed.

2.16. Protein corona detection

Samples were prepared following an adjusted protocol from Dilliard et al. [34] 50 µl fresh LNP samples (1:2 with HPW) and reconstituted SD-LNPs (5 mg/ml Lactose) were incubated with human BALF for 15 min at 37 °C at a volumetric ratio of 1:1. After incubation, samples were loaded onto 300 µl sucrose cushion (0.7 M) and centrifuged at 15,300 G at 4 °C for 1.5 h. Afterwards supernatant was removed and washed with 1× PBS and centrifuged at 15,300 G at 4 °C for 5 min. This washing step was performed twice more. LNPs and corona were kept dry at −20 °C upon MS analysis. A positive control of PBS with BAL was treated similar to our samples.

25 µl of 50 mM Hepes pH 8 containing 0.04 % n-Dodecyl-β-D-Maltoside were added per sample followed by incubation for 1 h at 60 °C shaking. After brief centrifugation 25 µl of enzyme solution were added (50 mM Hepes pH 8, 6 ng/µl Trypsin, 4 ng/µl LysC, 2 mM $CaCl_2$) followed by overnight incubation at 37 °C. Samples were acidified by addition of 5 µl of 1 % trifluoroacetic acid and stored at −20 °C.

Samples were measured on a TimsTOF Ultra2 mass spectrometer (Bruker) online coupled to an EvoSep One HPLC (EvoSep). 20 % of each sample was loaded on a EvoTip Pure (EvoSep) using the manufacturer's instructions, followed by automatic injection of the sample and separation on a PepSep C18 column (15cmx75µm, 1.9 µm; Bruker) using the 40SPD whisper zoom method at 50 °C column oven temperature. The DIA-Pasef method covered a mass range from 300 to 1250 *m/z* and a mobility range from 0.64 to 1.30 1/ko, with a ramp and accumulation time of each 100 ms. ICC 2.0 was switched on with 95 % target TIC. Precursor peptides were isolated using 27 variable MS/MS windows and 11 MS/MS ramps, resulting in a cycle time of 1.28 s. Collision energy for 0.6 1/ko was set to 20 and for 1.6 1/ko to 59.

Generated measurement files were quantitatively analyzed in the Spectronaut 19 software (Biognosis) in directDIA using BGS settings, disabling carbamidomethylation as fixed modification, disabling cross-run normalization, allowing for quantification on only proteotypic peptides and applying the QUANT2.0 label-free quantification method allowing for a mean TOP3 protein group quantity calculation. Searches were performed using the canonical Swissprot Human (20,432 sequences) database. TOP3 protein group quantities were imported in Perseus 2.0.11 software (MPI Martinsried). Abundances were log2 transformed and the data was filtered for at least 5 valid values per protein in all samples. Missing values were imputed from normal distribution using default settings. The average quantities per protein per group were calculated and used for ratio calculations and group comparisons applying a Student's *t*-test.

2.17. Statistical analysis

If not stated otherwise, experiments were performed in triplicates, and results are represented as mean ± s.d. Violin plots were used, where every data point of the measurements or simulations was considered; the median with quartiles is shown. The normality distribution of experimental data was tested using the Anderson-Darling and Shapiro-Wilk tests. One-way ANOVA (with the Tukey post-hoc test) was performed in GraphPad Prism (GraphPad Software, La Jolla, USA, v. 10.4.1) to calculate the *p*-values with 95 % confidence. Affinity Designer 218.2 (version 2.5.7, Serif Ltd., West Bridgford, UK), PyMOL (version 2.5.8, Schrödinger Inc., New York, NY, USA), and GraphPad Prism were used for visualization.

3. Results and discussion

3.1. Spray-drying induces alterations in LNP characteristics

To assess whether the structural changes observed in SD RNA-LNPs upon rehydration result from reversible sugar–membrane interactions or more permanent stress-induced modifications, Onpattro-like LNPs were spray-dried as a suspension containing 0.4 mg/ml LNPs and 50 mg/ml lactose (Fig. 1A). After spray drying, the powder was resuspended in RNase-free water to reach the starting concentration and subsequently dialyzed against PBS at room temperature for up to 24 h. For controls, fresh LNPs in PBS and a fresh suspension equivalent to the spray-dried formulation (0.4 mg/ml LNPs, 50 mg/ml lactose) were dialyzed under identical conditions.

No significant changes were observed in the control LNPs, indicating that incubation with lactose alone did not impact particle integrity. In contrast, SD in the presence of lactose led to a substantial increase in particle size. Dynamic light scattering, as in previous studies (Supplementary Fig. 1 A), and nanoparticle tracking analysis (NTA) (Fig. 1B, C) both confirmed a shift toward larger hydrodynamic diameters, with NTA revealing upward shifts in both mean (Supplementary fig. 1B) and median (D50) size as well as in D90 values. The size distribution also broadened, which indicates increased heterogeneity among particles. Detailed analysis of the D90 population (Fig. 1C) showed that while a subset of SD LNPs underwent substantial enlargement, approximately three-quarters of the population remained within the original D90 range.

Importantly, dialysis for 24 h did not reverse the size increase, implying that the changes were not due to loosely bound lactose but rather to irreversible structural modifications in membrane organization [4]. This finding is consistent with previous reports of persistent sugar coatings on Comirnaty LNPs detectable by NMR [35] and supported by desiccation studies showing that removal of sugars from lipid membranes required significant energy input [36].

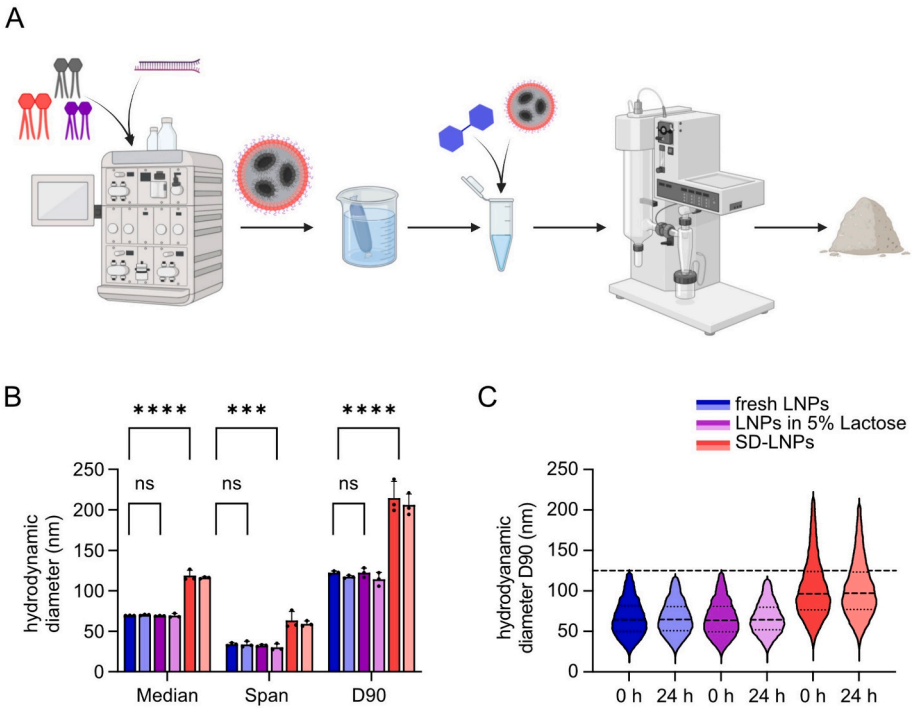

Fig. 1. Dialysis of Onpattro-like LNPs after SD. A) SD-based process for the manufacturing of dry powder RNA-LNPs. B) Hydrodynamic diameter of redispersed LNPs before (dark) and after (lighter) 24 h dialysis against PBS, measured via NTA. C) D90 values from size measurements by NTA for fresh LNPs, LNPs in 5 % lactose, and SD LNPs before (dark) and after (lighter) dialysis. Data points indicate mean ± s.d. ($n = 3$, with individual replicates in bar diagrams shown as points. Violin plots represent the distribution of all individual particle sizes within the D90 range; the median and quartiles are indicated (n = 3). Statistical analysis was performed using one-way ANOVA: ns, $p > 0.05$; *$p < 0.05$; **$p < 0.01$; ***$p < 0.001$; ****$p < 0.0001$.

To further investigate membrane organization, we employed Laurdan, a fluorescent probe that reports on lipid packing and hydration. In line with the observations on size and size distribution, fresh LNPs and control samples dialyzed with lactose exhibited comparable generalized polarization (GP) values. However, SD LNPs displayed a marked increase in GP (Supplementary Fig. 1C), indicative of reduced membrane hydration and enhanced lipid packing.

Collectively, these data demonstrate that SD induces lasting, irreversible modifications in RNA-LNPs, characterized by stress-induced size increases, membrane rigidification, and partial particle heterogeneity. These alterations are consistent with the water replacement hypothesis, whereby sugars substitute for water molecules at the lipid headgroups, promoting increased lipid spacing and potential membrane thinning [37].

3.2. *Lactose interacts with components of the LNP membrane*

To investigate the molecular basis of lactose–membrane interactions, we performed all-atom molecular dynamics simulations (MDS) using bilayer LNP-membrane models, hereafter referred to as membranes. Modelling the LNP surface as a bilayer allowed us to approximate its interfacial organization while keeping computational costs manageable. This approach follows previous studies that explored the influence of disaccharides, such as trehalose, on LNP membranes under different hydration states [38–42]. Our focus was specifically on the behaviour of lactose after SD. LNP membranes were simulated under three conditions: (i) fully hydrated, (fresh LNPs in lactose solution); (ii) nearly dehydrated (SD-LNP); and (iii) rehydrated (resolvated LNPs after spray drying).

Modelling the LNP surface as a bilayer, however, necessitates consideration of surface composition. Recent studies employing Cryo-TEM [43], NMR [35,44], and MDS [45] suggest that PEG-lipids and DSPC are enriched at the LNP periphery, while the core is densely packed with cholesterol and ionizable lipids. Given the uncertainty of the surface composition, we simulated membranes containing varying D-Lin-MC3-DMA (MC3) concentrations (corresponding to 50 %, 5 %, or 0 % MC3 molecules per leaflet) to reflect the spectrum of possible LNP surface compositions.

Analysis of the simulation trajectories revealed free diffusion of lactose molecules in both hydrated and rehydrated systems after approximately 1 ns, as confirmed by linear increases in mean square displacement (MSD) (Supplementary Fig. 2 A–C). Notably, MSD values were lower in rehydrated compared to hydrated systems, suggesting stronger lactose–membrane association after reconstitution. Examination of representative endpoint snapshots (5 % MC3 membranes, after 10 ns) supported these findings (Fig. 2A-C). In fully hydrated systems, lactose molecules (black) remained primarily associated with PEG-DMG-2000 (violet) in the aqueous phase. In contrast, following dehydration and rehydration, lactose localized closer to DSPC-rich (red) membrane regions, in some cases penetrating the bilayer interior.

Mass density distributions (5 % MC3 membranes: Fig. 2D-F, 50 %, 0 % MC3 membranes: Supplementary Fig. 2D—I) revealed distinct lactose peaks within membranes after dehydration, consistent with clustering, while rehydrated membranes showed broader, less defined distributions, which indicates partial dissolution of clusters. Quantification by area under the curve (AUC) analysis of radial distribution functions (Supplementary Fig. 3 A–C) confirmed these trends: lactose–membrane proximity was highest after dehydration, decreased after rehydration, but did not fully revert to hydrated levels. These results support a model in which dehydration enhances lactose–membrane interactions via water replacement mechanisms, with partial persistence upon rehydration.

Lactose integration into membranes was evident across all simulations, which aligns with previous findings [37]. Analysis of symmetrized mass density distributions (Supplementary Fig. 2 J) demonstrated a decrease in membrane density in dehydrated and rehydrated systems,

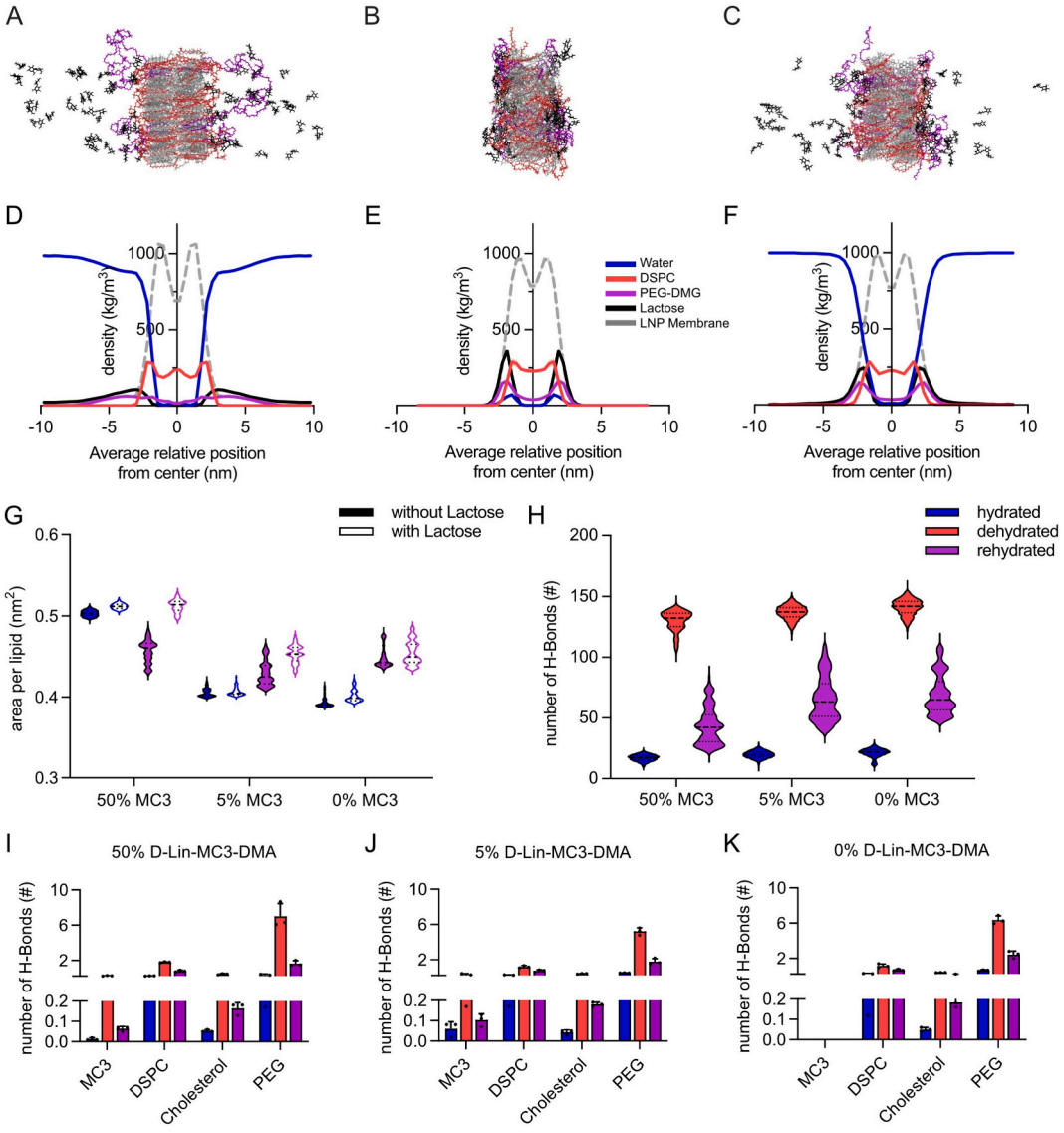

Fig. 2. All-atom molecular dynamics simulations (MDS) of LNP membrane models at different hydration states. A–C) Representative snapshots of A) hydrated LNP membrane formulation before spray drying (SD), B) SD LNP membrane formulation (dehydrated), and C) rehydrated SD LNP membrane formulation containing 5 % MC3 (i.e., 5 of 100 total lipids are MC3) after 10 ns of simulation. Lactose (black), MC3 (gray), cholesterol (gray), DSPC (red), and PEG-DMG-2000 (violet) are shown; water and ions are omitted for clarity. D—F) Symmetrized mass-density profiles relative to the center of the simulation box for lactose, LNP membrane components, DSPC, and PEG-DMG-2000 in hydrated (D), dehydrated (E), and rehydrated (F) systems containing 5 % MC3. G) Area per lipid for LNP membranes simulated with and without lactose, shown as violin plots from 1 ns to 10 ns (data sampled every 2 fs). H) Number of hydrogen bonds between lactose and different LNP membrane components, shown as violin plots from 1 ns to 10 ns (sampled every 4 fs). I—K) Mean normalized number of hydrogen bonds between lactose and individual LNP membrane components. Data are shown as mean ± s.d. for panels D—F and I—K, with individual replicates in bar diagrams shown as points, or as median with quartiles for panels G and H ($n = 3$). (For interpretation of the references to colour in this figure legend, the reader is referred to the web version of this article.)

particularly in 0 % and 5 % MC3 membranes, where DSPC and PEG content were highest. To further quantify this effect, additional simulations compared membranes with and without lactose under hydrated and rehydrated conditions. The area per lipid, calculated over 9 ns in NPT ensembles, was consistently higher in lactose-containing membranes, with the greatest differences observed after rehydration (Fig. 2G). Membranes without lactose exhibited higher post-rehydration densities (data not shown), reinforcing the notion that lactose integration leads to membrane thinning. These observations align with the water replacement theory, which proposes that sugars stabilize membranes by occupying the space between lipid headgroups [37,46]. Literature reports using small-angle neutron scattering (SANS) demonstrated that sugars at low concentrations (<0.2 M) strongly bind to bilayers, inducing membrane expansion and thinning [37,40]. Given that lactose concentrations during SD were below 0.2 M, similar mechanisms likely underlie our observations.

Hydrogen bonding represents another key molecular interaction underlying lactose–membrane association. Calculation of hydrogen bonds over the final 9 ns of simulations revealed an increase upon dehydration, followed by a slow and incomplete decrease after rehydration (Fig. 2H). Among lipid components, DSPC and PEG-DMG-2000 accounted for the majority of hydrogen bonding with lactose (Figs. 2I–K), consistent with their surface exposure. The high affinity of PEG-DMG-2000 is attributed to its multiple polyethylene glycol monomers, which serve as efficient hydrogen bond acceptors. The prominent interaction with DSPC indicates its high availability at the membrane surface, consistent with prior MDS and NMR studies of LNP structure [45]. The slow dissociation and persistence of sugar–lipid hydrogen bonds following rehydration has been reported in previous studies combining MDS with Fourier-transform infrared (FTIR) and two-

dimensional infrared (2D-IR) spectroscopy. These studies demonstrated that sugar–lipid hydrogen bonds are stronger and more durable than water-lipid hydrogen bonds [38]. These findings, validated experimentally by Viera et al., support a model where sugars protect membranes during dehydration stress via water replacement, with bond dissociation being a slow, energetically demanding process [36].

Combined, these results demonstrate that dehydration promotes enhanced lactose–membrane interactions via hydrogen bonding and partial membrane integration. DSPC and PEG-DMG-2000, abundantly present on the surface of LNPs [44,47], were identified as principal sites of interaction.

3.3. Varying PEG and DPSC concentrations in LNPs modulate lactose interactions

Given the central role of DSPC and PEG-lipids in mediating lactose–membrane interactions in simulations, we next investigated how variations in LNP surface composition affect structural changes upon SD. Four distinct LNP formulations were generated, differing in DSPC and PEG content (Table 1), and subsequently subjected to SD. To control for inherent compositional effects on particle size (particularly driven by the PEG content [48]), membrane fluidity (e.g., influenced by the cholesterol content [49]), and apparent pKa, differences between pre- and post- SD values are discussed as relative changes.

Across all formulations, SD induced an increase in hydrodynamic diameter and PDI (Fig. 3A, B). Notably, LNP 4, which is characterized by the highest DSPC and PEG content, exhibited the most pronounced size increase and variability. This is not only consistent with our simulation results revealing that both PEG and DSPC strongly influence lactose interactions at the outer LNP shell but also aligns with prior studies indicating that sugars preferentially associate with phospholipid headgroups through hydrogen bonding and water replacement mechanisms [36,37,50–53]. As mentioned previously, cholesterol also influences membrane rigidity and stability, and the lower cholesterol content in LNP 4 could further affect its stability during spray drying. However, this effect appears to be limited, as LNP 2, despite its similarly low cholesterol content, showed no significant difference in size increase compared to LNP 1, which contains a higher cholesterol fraction. This suggests that cholesterol depletion alone is not the dominant factor. Rather, the combination of high DSPC and PEG content in LNP 4 likely amplifies these effects by altering interfacial organization and mechanical stability during spray drying.

For all LNPs, GP values increased after SD (Fig. 3C), reflecting reduced membrane hydration and greater lipid ordering. Notably, LNPs with lower initial DSPC content (LNP 1 and LNP 3) displayed a more substantial relative increase in GP, suggesting that membranes with initially lower order are more susceptible to SD-induced rigidification. Absolute GP values after drying, however, remained highest for formulations rich in DSPC (Supplementary Fig. 4), supporting the notion that lipid composition pre-defines baseline membrane organization. In

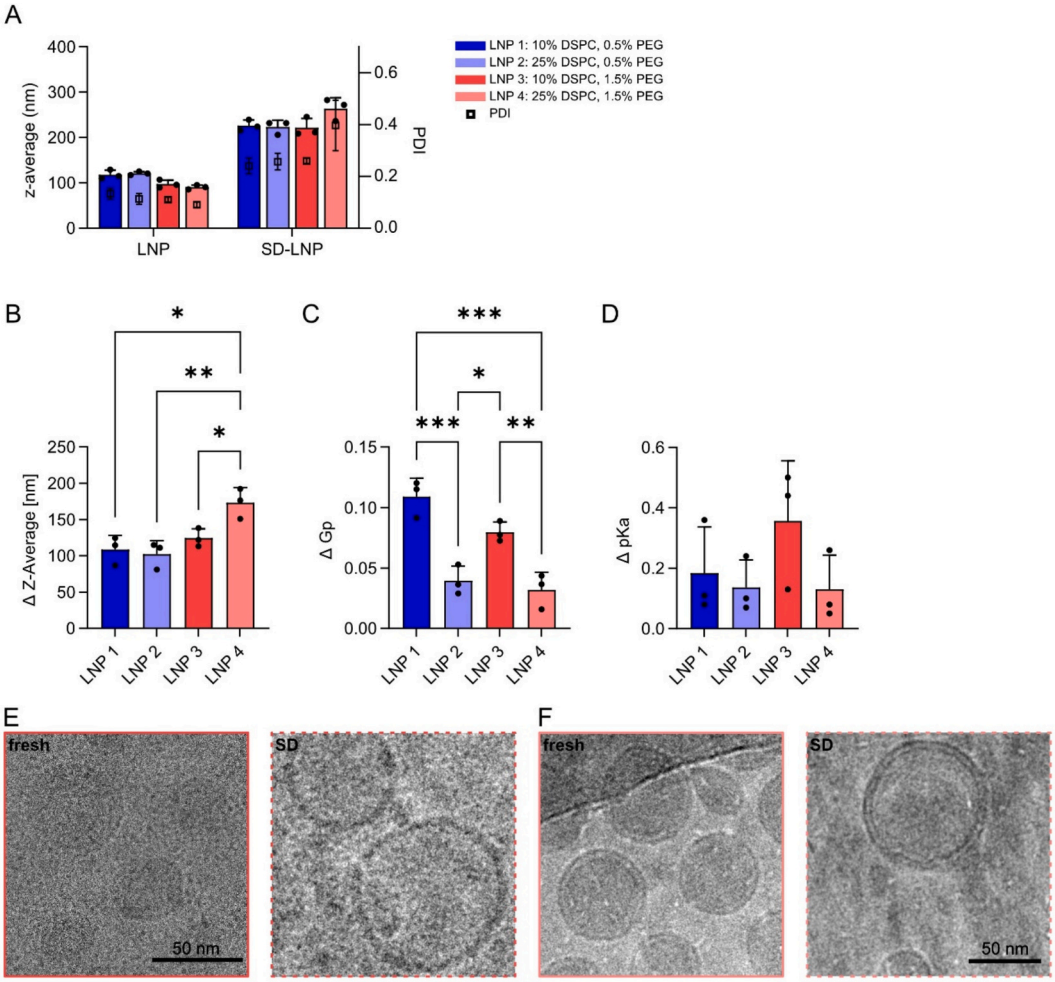

Fig. 3. Physical characteristics of LNPs after SD. A) DLS Data before and after SD of all four formulations. Difference in B) *Z*-Average, C) Gp value, and D) apparent pKa value of LNPs before and after SD. *E*-F) cryo-TEM micrographs of LNP3, LNP3 after SD (E), LNP 4 and LNP 4 after SD (F). Data points indicate mean ± s.d. ($n = 3$), with individual replicates in bar diagrams shown as points. One-way ANOVA, ns, > 0.05, *, $p < 0.05$ **, $p < 0.01$, ***, $p < 0.001$, ****, $p < 0.0001$.

contrast to the findings by Orlikowska-Rzeznik et al., who demonstrated that high cholesterol contents in membranes elevate Gp values, higher cholesterol contents in LNP 1 and LNP 3 did not correlate with higher absolute Gp values. This likely reflects the distinct structural organization of LNPs, in which cholesterol predominantly resides in the internal core complexed with ionizable lipids and RNA, resulting in limited or stable cholesterol presence at the outer membrane surface probed by Laurdan.

These experimental results corroborate our simulation data, where an increase in area per lipid was observed after dehydration and rehydration (Fig. 2G), indicative of membrane expansion. Changes in the area under the curve (AUC) of mass density profiles between hydrated and rehydrated membranes (Supplementary Fig. 2E) further suggested membrane thinning or reorganization. Symmetrized density analyses (Fig. 2F) confirmed these trends, revealing greater localization of lactose within or directly atop the membrane after rehydration. Notably, an increased presence of DSPC near the membrane surface was detected in rehydrated systems, particularly in the 5 % and 0 % MC3 simulations. Consistently, the persistent elevation of GP after rehydration supports the notion that lactose partially integrates into the membrane, altering lipid packing and organization after drying.

To probe surface reorganization, apparent pKa values were determined by TNS assay. In LNPs, the pKa is influenced by both, the presence of protonated ionizable lipid in the outer layer, and by the environment in which the ionizable lipid is situated. Here, while shifts were less pronounced than changes in GP, a consistent trend toward lower apparent pKa values after SD was observed across all formulations (Fig. 3D), indicating modified surface environments, potentially due to altered ionizable lipid exposure or local dielectric properties.

The most pronounced structural alterations, observed in LNP 3 and LNP 4, were visualized by cryo-TEM (Fig. 3E and F). In fresh Onpattro-like LNPs (LNP3, Fig. 3E), monodisperse particles of ~50 nm with partially lamellar or multilamellar interiors were observed. Post-SD, LNP 3 exhibited increased size heterogeneity, with a notable fraction of particles exceeding 200 nm (Fig. 3E, Supplementary Fig. 5), consistent with DLS (Fig. 3A) and NTA data (Supplementary Fig. 6B—C). A dark, electron-dense ring surrounding the particles was detected, reminiscent of previously reported changes in LNP structure post-SD[4]. Micrographs revealed partial lamellar organization for some non-dried LNP 4 particles, likely due to the elevated DSPC content. Most LNPs displayed the previously reported distinct unilamellar structure typical for siRNA-LNPs formulated at an N/P ratio of 3 [54], consistent with the relatively higher baseline GP values of LNP 4 compared to LNP 3 (Fig. 3F and Supplementary Fig. 5). After SD, LNP 4 particles frequently appeared elliptical, occasionally exhibiting polymorphic, fused, or bleb-like structures (Fig. 3H, Supplementary Fig. 5). This observation is consistent with prior reports linking dehydration of LNPs during freeze drying with bleb formation [55]. In contrast to SD LNP 3, LNP 4 particles lacked a distinct, dark electron-dense outer layer (Fig. 3E, F and Supplementary Fig. 5). Although some membrane-associated material remained visible, it appeared less prominent than in LNP 3, consistent with the smaller GP and pKa shifts observed for LNP 4 after drying. This suggests that membrane reorganization was less extensive in DSPC-rich LNPs. Nevertheless, morphological changes—including increased particle size, fusion events, and structural heterogeneity—were more pronounced in LNP 4 than in LNP 3, reflecting reduced mechanical stability during dehydration and rehydration at higher DSPC content. These findings were further corroborated by NTA data showing a larger particle population after SD (Supplementary Fig. 6C).

Collectively, our results demonstrate that the extent and nature of lactose–membrane interactions—and the resulting structural consequences—are strongly dependent on LNP surface composition, particularly DSPC and PEG-lipid content. Further elucidation would benefit from SAXS or SANS analyses, which, however, are beyond the scope of the present study.

3.4. Spray-drying affects LNP internalization and gene silencing efficiency

To assess the biological relevance of the structural alterations identified above, we next evaluated their influence using dedicated biological models, i.e., performance in in vitro lung models and penetration studies in artificial mucus.

RNA-LNPs enter cells via endocytosis, which through receptor-mediated pathways (e.g., clathrin- or caveolin-mediated endocytosis, CME) or receptor-independent routes such as macropinocytosis and phagocytosis [56,57]. The efficiency of cytosolic delivery depends on the entry mode, which is influenced by both particle properties and cell type. Receptor-mediated endocytosis predominates and is facilitated by a protein corona formed around the LNPs upon serum exposure. Components of this corona include apolipoprotein E (ApoE), which binds to low-density lipoprotein receptors (LDLR) [58], as well as high-density lipoprotein (HDL) [59], and albumin [60]. Protein corona formation is dynamic, with PEG-lipid dissociation [61], further promoting protein adsorption and thereby nanoparticle-cell interactions.

To determine the impact of lipid composition and SD on LNP behaviour, we evaluated all formulations for cellular uptake and eGFP silencing in H1299-eGFP cells. Cellular uptake of fresh and reconstituted SD LNPs and eGFP protein levels were monitored at various time points post-transfection to capture subtle differences in uptake kinetics. Notably, PEG-shedding and protein corona formation are known to occur within 30 min of serum exposure [61] with gradual accumulation of siRNA-LNPs in endosomes reported within the first 4–6 h post-uptake [62].

LNP 1, with a PEG-lipid content of 0.5 %, exhibited rapid and high uptake, likely due to fast PEG shedding and efficient protein corona formation. In contrast, LNP 2, despite having the same PEG-lipid content, achieved only 20 % of the uptake observed for LNP 1 after 24 h. LNP 3, with a higher PEG-lipid content, i.e., 1.5 %, also showed efficient uptake over 24 h, though with a slight delay attributed to a prolonged PEG-shedding process. A reduction in MFI at 16 h for LNP 1 and LNP 3 suggested the onset of exocytosis [63] (Fig. 4A, C). Contrary to initial expectations, LNP 4, which combines high PEG and DSPC content, exhibited uptake levels twice those of LNP 2, although still only one-third that of LNP 1. LNPs with 25 % DSPC content consistently underperformed compared to those with 10 % DSPC. Uptake efficiency correlated strongly with GP values, indicating that sufficient hydration and a less ordered lipid state are critical for effective internalization (Supplementary Fig. 4). For SD formulations, uptake was significantly reduced across all groups. LNP 1 retained only ~10 % of its fresh formulation uptake efficiency, LNP 2 (28 %), LNP 3 (27 %), and LNP 4 (53 %). This decline may result from membrane-associated lactose and membrane reorganization during drying, which likely alter protein corona formation on the LNP surface. Comparative analysis revealed that formulations showing minimal changes in GP value before and after SD experienced smaller relative losses in uptake. Additionally, it cannot be ruled out that the SD process impacted the fluorophore Alexa Fluor 647, potentially contributing to the observed reduction in signal intensity. Cellular uptake performance was further visualized by confocal microscopy 4 h post-transfection (Fig. 4).

Effective silencing depends not only on cellular uptake but also on efficient endosomal escape of siRNA, regarded as a bottleneck within RNA delivery [64]. Studies indicated that, for many routinely used ionizable lipids, only 1–3.5 % of siRNA internalized by endocytosis reaches the cytosol; once released, siRNA can exert its effect within 10 min [62,65]. The specific gene silencing efficiency of eGFP-siRNA encapsulating LNPs only, was monitored prior to the determination of the kinetic exemplary for fresh and reconstituted SD LNP 3 encapsulating either eGFP-siRNA or scrambled siRNA as a negative control (NC), free siRNAs and lactose control groups (Supplementary Fig. 8). Investigating the gene silencing efficiency of the different formulations show an exponential decay in eGFP expression for all fresh LNP formulations. LNP 1 and LNP 3 achieved the fastest knockdown within 24 h, whereas

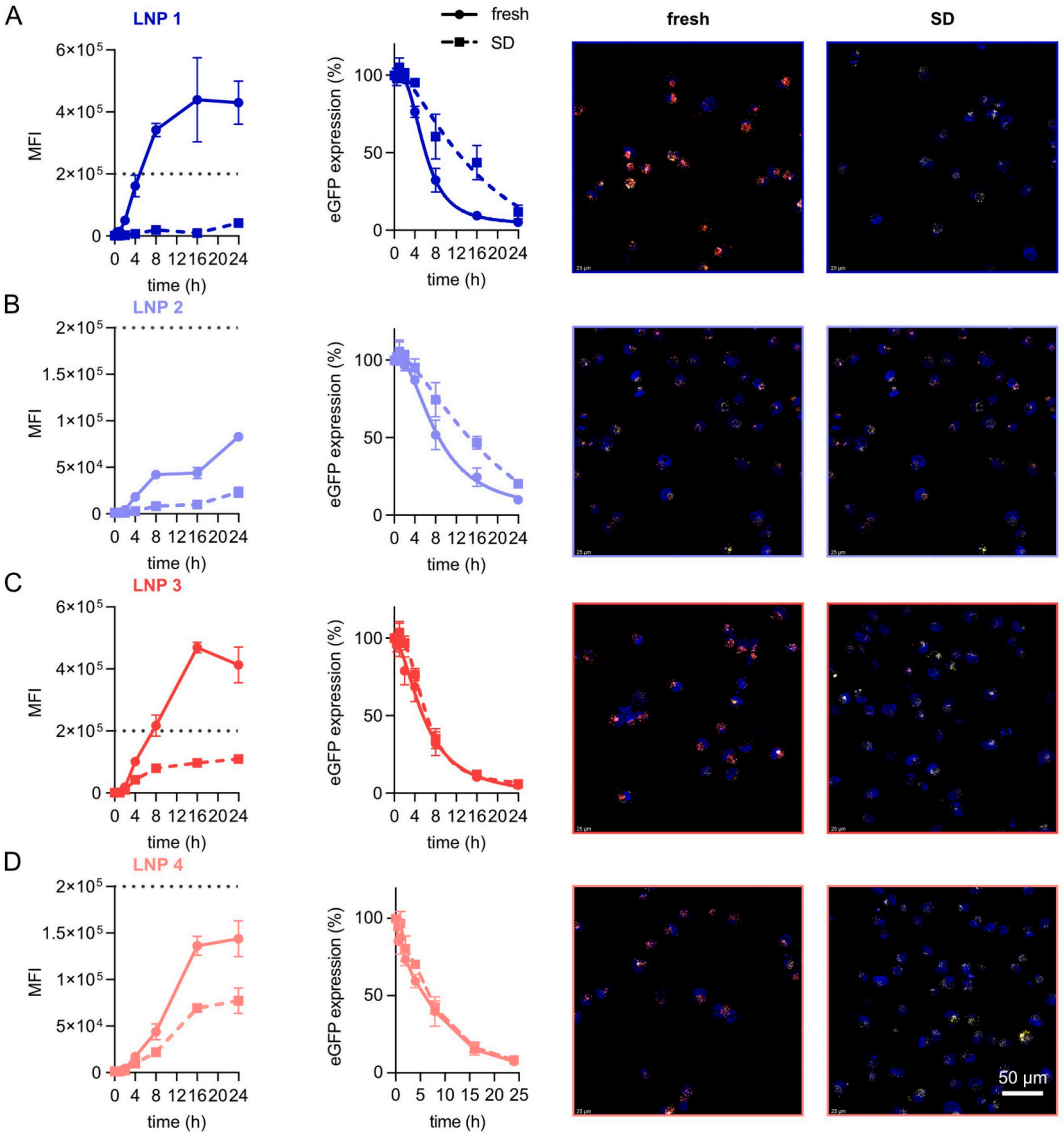

Fig. 4. In in vitro performance evaluation post-SD. Cellular uptake and eGFP gene silencing of LNP formulations 1–4 (A-D) before and post-SD. Cellular uptake (column 1) und eGFP protein downregulation (column 2) in H1299-eGFP treated with formulations containing AF647-labled eGFP-siRNA analyzed simultaneously by flow cytometry 0.5, 1, 2, 4, 8, 16 and 24 h post transfection. Data points indicate mean ± s.d. ($n = 3$). Visualization of cellular uptake 4 h post transfection by confocal laser scanning microscopy (column 3, 4). Images are presented as merge pictures (blue: nuclei staining with DAPI, yellow: endosomal staining with LysoTracker red DND-99, red: AF647-labled siRNA). (For interpretation of the references to colour in this figure legend, the reader is referred to the web version of this article.)

LNP 2 and LNP 4 exhibited delayed silencing, reaching 90 % reduction only after 16 h. This tailing effect likely results from the slower and lower particle uptake observed for these formulations and may also reflect the reduced fusogenic efficiency reported for LNPs with high DSPC content [66]. After 24 h, all formulations achieved >90 % eGFP downregulation.

For the SD LNPs, formulations LNP 3 and LNP 4 retained knockdown kinetics comparable to their fresh counterparts. Despite reduced uptake, their colloidal and fusogenic properties appear preserved, yielding similar silencing efficiencies. In contrast, LNP 1 and LNP 2 exhibited markedly reduced knockdown efficiency across the observation period, reaching only 88 % (LNP 1) and 80 % (LNP 2) after 24 h. Analysis of knockdown half-time highlighted a pronounced change: the time to achieve 50 % eGFP reduction increased from 5.8 h to 16.7 h for LNP 1, and from 8.2 h to 19.8 h for LNP 2 following SD (Supplementary Table 2). This performance drop is partly attributable to lower cellular uptake. It is also plausible that thermal stress and shear forces during drying disproportionately affected these two formulations, which contained only 0.5 % PEG-lipid. It was reported that LNPs with 1 % PEG exhibited superior colloidal stability compared to 0.5 % PEG, even at temperatures as high as 90 °C [67]. Similarly, in the context of nebulization, higher PEG-lipid content conferred improved resistance to shear stress. As such, siRNA integrity may have been partially compromised, or material loss may have occurred during processing.

3.5. *Complex lung barriers expose formulation-specific differences in LNP transport and transfection efficiency*

Following inhalation and deposition in the airways, LNPs must traverse the airway mucus layer before reaching and entering pulmonary epithelial cells. This viscoelastic barrier consists of a mucus gel layer overlaying a ~ 5–20 µm-deep periciliary layer, with the thickness of the mucus layer increasing from distal to proximal regions of the lung [68,69]. Mucins, primarily MUC5AC and MUC5B, form a mesh-like

network with pore sizes reported to range from 100 to 500 nm[70]. In healthy individuals, airway mucus comprises approximately 97 % water and 3 % solids, including mucins, non-mucin proteins, salts, lipids, and cellular debris, with mucins accounting for less than 30 % of the solid fraction [69,71]. In disease states, such as mucin hypersecretion or surface liquid depletion, the total solid content can increase to 15–20 %.

With a mass median diameter (MMD) 4.86 ± 0.13 μm and 4.26 ± 0.13 μm exemplary assessed for SD LNP 3 and SD LNP 4 (Supplementary Fig. 11) our dry powders show good inhalable properties and are within the desired particle size range between 1 and 5 μm suitable for pulmonary administration [72]. To assess LNP transport under physiologically relevant yet experimentally tractable conditions, we adapted an artificial mucus model containing 0.5 % mucin and ~ 1 % additional non-mucin solids [31]. Critically, the reduced concentration ensures a homogeneous, fully solubilized gel phase, essential for reproducibility in in situ transport assays. Importantly, mucin and total organic content were maintained above the polymer overlap concentration, estimated at ~0.06 % mucin oligomers or ~ 0.18 % organic solids in airway mucus [71], ensuring a semidilute regime with relevant polymer network properties. Thus, although the total solid content is lower than that of native mucus, the model exhibits viscosity values (Supplementary Fig. 12) within the range reported for healthy human airway secretions [73].

To assess LNP transport this mucus model barrier, we employed a transwell-based assay using 6.5 mm inserts coated with 50 μl of artificial mucus, yielding an estimated layer thickness of 1.51 mm—approximately 100-fold thicker than physiological airway mucus. (Fig. 5A).

Despite this exaggerated barrier, >85 % of freshly prepared LNPs traversed the mucus layer within 2 h (Fig. 5C). PEGylation is widely associated with improved mucus diffusion due to its hydrophilic and near-neutral surface properties in sub-200 nm nanoparticles [74]. However, in this system, the effect of PEG-lipid content could not be reliably assessed, as substantial inter-replicate variability obscured any clear trends. This variability likely stems from inconsistent mucus deposition and uneven meniscus curvature introduced by capillary forces, resulting in non-uniform barrier thickness across transwells. In contrast, the impact of SD on mucus penetration was pronounced for most formulations. After 24 h, all SD LNPs except LNP 1 (100 % recovery) showed reduced translocation: LNP 2 (85 %), LNP 3 (72 %), and LNP 4 (73 %) (Fig. 5C). These findings likely reflect increased hydrodynamic diameters post-SD, which may hinder diffusion through the sterically restrictive mucin mesh, reaffirming particle size as a dominant determinant of mucus mobility.

To independently quantify nanoparticle mobility, we employed fluorescence correlation spectroscopy (FCS) to determine diffusion coefficients in buffer and artificial mucus (Fig. 5D). In PBS, freshly prepared formulations showed a narrow range of median diffusion

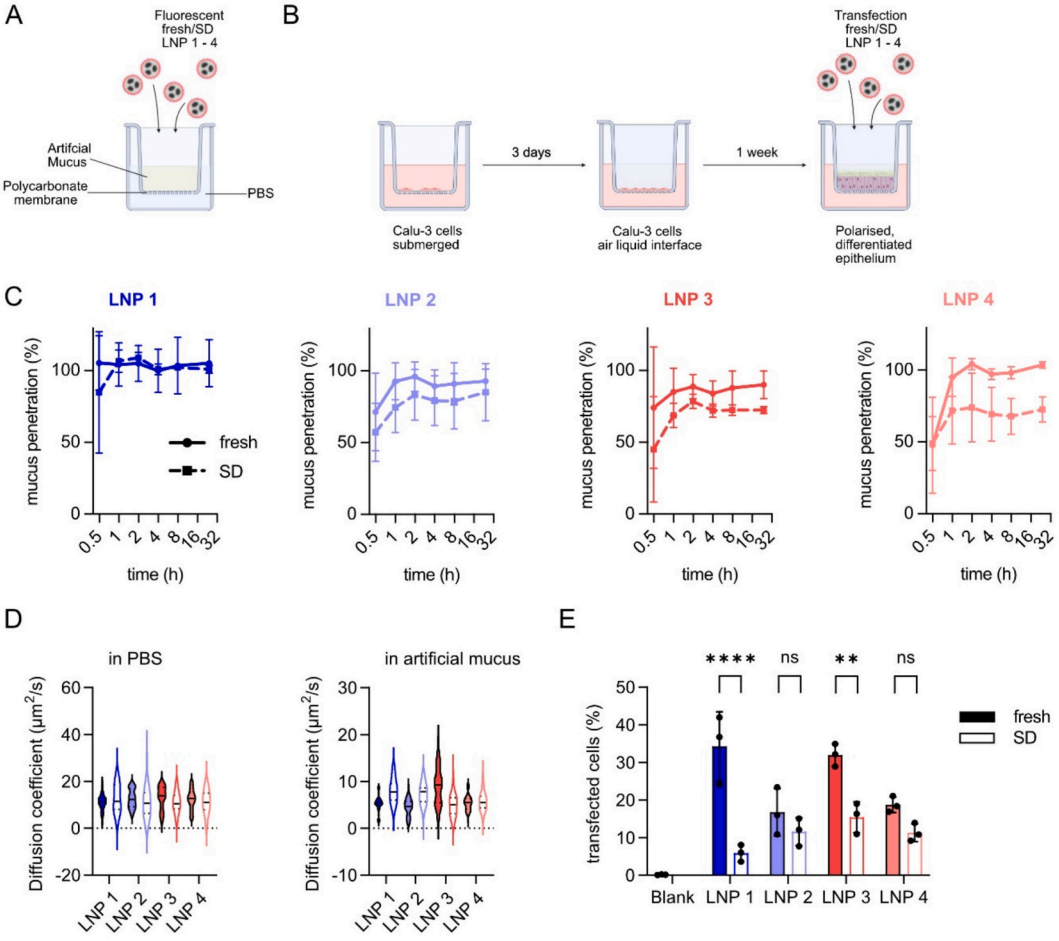

Fig. 5. LNP transport through artificial mucus and transfection efficiency in ALI. A) Schematic representation of a Transwell mucus penetration assay. B) Schematic of Calu-3 cells seeded into a Transwell. After three days confluence was reached and air lift performed. After one week polarized and differentiated Epithelium was transfected with 160 pmol fresh and SD AF647-labled siRNA LNPs 1–4. C) Transwell mucus penetration assay of LNP 1–4 fresh and spray dried. D) Diffusion coefficient measurements of fresh and spray dried LNP 1–4 in PBS and artificial mucus via FCS. Box plots are created from a minimum of 20 technical replicates. E) Transfected ALI cells (%) of fresh and SD LNPs 1–4 after 6 h. Blank samples were treated with PBS. Data points indicate mean ± s.d. ($n = 3$ technical replicates), with individual replicates in bar diagrams shown as points. One-way ANOVA, ns, > 0.05, *, $p < 0.05$ **, $p < 0.01$, ***, $p < 0.001$, ****, $p < 0.0001$.

coefficients—from 11.3 $\mu m^2/s$ (LNP 1) and 12.3 $\mu m^2/s$ (LNP 2) to 13.9 $\mu m^2/s$ (LNP 3) and 12.8 $\mu m^2/s$ (LNP 4)—consistent with minor differences in PEG content and particle size. A slight but detectable decrease in mobility was observed post-SD across all formulations, aligning with the size increase noted after processing.

When measured in artificial mucus, diffusion coefficients dropped substantially, reflecting hindered transport through the mucin network. Fresh formulations showed mean diffusion coefficients of 5.4 $\mu m^2/s$ (LNP 1), 4.7 $\mu m^2/s$ (LNP 2), 9.3 $\mu m^2/s$ (LNP 3), and 5.5 $\mu m^2/s$ (LNP 4). Notably, LNPs 3 and 4—containing higher PEG content—retained better mobility, consistent with their smaller size and more hydrophilic surface. Upon redispersion post-SD, the trend partially inverted: LNPs 1 and 2 showed increased mobility (7.8 $\mu m^2/s$ each), while LNP 3 decreased to 5.1 $\mu m^2/s$, and LNP 4 remained largely unchanged These complex patterns cannot be fully explained by size alone. It is plausible that PEG desorption, changes in lactose association, and protein adsorption from the mucus synergistically influence post-SD diffusivity. We note that FCS in mucus may reflect contributions from non-Brownian effects, due to transient trapping and microheterogeneity in the mucus mesh, which may limit precise interpretation of absolute diffusion values. Further investigation is required to dissect these factors. Nevertheless, all formulations exhibited sufficient mobility to theoretically traverse a 25 μm mucus layer within two minutes—well below typical mucociliary clearance timescales. However, it should be noted that our artificial mucus model represents a lower bound of solid content; in patients with hyperconcentrated or pathologically altered secretions, LNP diffusivity may be substantially impaired, as reported previously [70].

While 2D cultures provided insights into cellular uptake and gene silencing kinetics (Section 3.4), and the transwell setup and FCS measurements enabled isolated assessment of mobility in mucus, neither model fully captures the complexity of the airway barrier in vivo. To integrate these aspects, we next evaluated LNP performance in a physiologically relevant air–liquid interface (ALI) culture system.

Calu-3 cells were cultured under ALI conditions to promote differentiation into a polarized epithelial monolayer that recapitulates key features of the bronchial airway, including mucus secretion, tight junction formation, receptor expression, and cytokine production (Fig. 5B). ALI cultures are notoriously difficult to transfect [75,76], a challenge attributed to both the physical mucus barrier and diminished protein corona formation, which can limit receptor-mediated internalization. Transfection efficiency was quantified after 6 h exposure to either fresh or SD LNPs. The observed trends closely mirrored those obtained in 2D cultures. Among fresh formulations, LNP 1 (34 %) and LNP 3 (32 %) achieved the highest transfection rates, whereas LNP 2 (12 %) and LNP 4 (19 %) performed less efficiently. The SD formulations followed a similar rank order, with LNP 3 outperforming others, followed by LNP 2, LNP 4, and LNP 1, which exhibited the lowest efficiency post-drying (Fig. 5E).

Notably, the relative decline in transfection upon spray-drying was attenuated in ALI cultures compared to H1299 cells. LNP 1 retained 17 %, LNP 2 69 %, LNP 3 48 %, and LNP 4 60 % of the efficiency of their fresh counterparts. These findings suggest that uptake pathways in ALI cultures may rely less on corona-mediated mechanisms and more on non-specific internalization routes.

Consistent with prior observations, transfection performance across formulations correlated with both absolute GP values and changes in GP following SD (Fig. 3C, Supplementary Fig. 4). This reinforces the hypothesis that formulations exhibiting minimal post-drying alterations in lipid order better preserve their cellular uptake and transfection efficiency.

3.6. Altered surface characteristics of LNPs influence protein-corona formation in human BAL fluid

Changes in lipid packing and surface chemistry can modulate nanoparticle interactions with biological fluids. Given the strong correlation between membrane order, post-drying stability, and uptake efficiency observed in vitro, we next assessed whether such alterations affect LNP identity at the pulmonary interface. To this end, we profiled protein coronas formed in human bronchoalveolar lavage fluid (BALF). Well-known work on SORT LNPs demonstrated that differences in lipid composition can indirectly govern organ-specific delivery by modulating protein corona formation in plasma, where adsorbed proteins act as endogenous targeting ligands [34,77]. Unlike plasma, BALF presents a distinct biochemical environment that, similarly to lung mucus, contains not only soluble proteins, but also surfactants, vesicles, nucleic acids, and cellular debris [69,78], yet it remains largely unexplored in the context of inhaled nanocarriers.

To address this, we profiled the protein coronas of fresh, and SD LNPs incubated in human BALF, freshly collected from a post-transplant donor under immunosuppressive therapy (male, 56 years old, never smoked), and corona-associated proteins were quantified by mass spectrometry. First, we generated an Upset plot [79] (Fig. 6A) comparing enriched proteins across all formulations. This analysis confirmed that each LNP recruited a distinct subset of BALF proteins, with stronger divergence observed after SD. In particular, SD-LNP3, SD-LNP4, and LNP4 shared a core set of proteins, consistent with their similar membrane order values (see Supplementary Fig. 4). In contrast, SD formulations displayed a broader range of unique enrichments than their fresh counterparts, indicating that altered surface properties post drying affect protein binding. Principal component analysis (PCA) revealed clear clustering by both LNP composition (LNP 3 vs. LNP 4) and processing status (fresh vs. SD, Supplementary Fig. 14), indicating that SD induces distinct shifts in corona profiles. These changes aligned with formulation-dependent differences in surface order (Gp-value), pKa, and cellular uptake described above.

Across all conditions, over 6200 proteins were identified. To isolate corona-specific enrichments, protein abundances were benchmarked against a BALF-only control processed in parallel. The top 20 enriched proteins (Fig. 6B) exhibited divergent patterns across formulations and processing states. For example, NADH-ubiquinone oxidoreductase chain 6 appeared prominently on fresh LNPs, whereas TLC domain–containing protein 4, a membrane-associated factor linked to lipid homeostasis, was enriched only on SD samples. Protein kinase C alpha, a DAG-sensitive signaling enzyme implicated in inflammation and proliferation, showed selective recruitment to DSPC-rich LNPs regardless of processing. While several proteins followed clear formulation-dependent trends, others, e.g., DNA repair protein XRCC1 or transcription factor IIH subunit XPD, exhibited variable, nonspecific enrichment.

To identify statistically significant shifts, we performed pairwise comparisons represented in volcano plots (Fig. 6C). SD LNPs recruited broader and more distinct protein subsets relative to their fresh counterparts. This effect was more pronounced for LNP 3 than LNP 4, mirroring their differential changes in membrane order and cellular uptake. Interestingly, while fresh LNP 4 displayed the most diverse protein enrichment, its SD counterpart showed reduced recruitment, whereas SD LNP 3 gained new protein interactions. These findings suggest that both lipid composition and physical processing shape the molecular fingerprint of LNPs at the lung interface.

Importantly, all measurements were normalized to a shared BALF control, eliminating artifacts arising from nonspecific background binding. The observation that corona composition tracks with physicochemical parameters, particularly membrane order, supports the broader hypothesis that post-processing stability governs biological performance. Notably, a 2023 meta-analysis summarized that only 0.3 % of published protein corona studies employed BALF, typically without reporting the specific specimen characteristics, and only a small fraction of these involved LNPs [80]. While previous work has examined protein corona formation in in vitro–produced mucus [81], this dataset, to the best of our knowledge, represents the first analysis of protein corona formation on LNPs in human BALF. Because BALF is patient-derived and highly heterogeneous in protein composition, we expect substantial

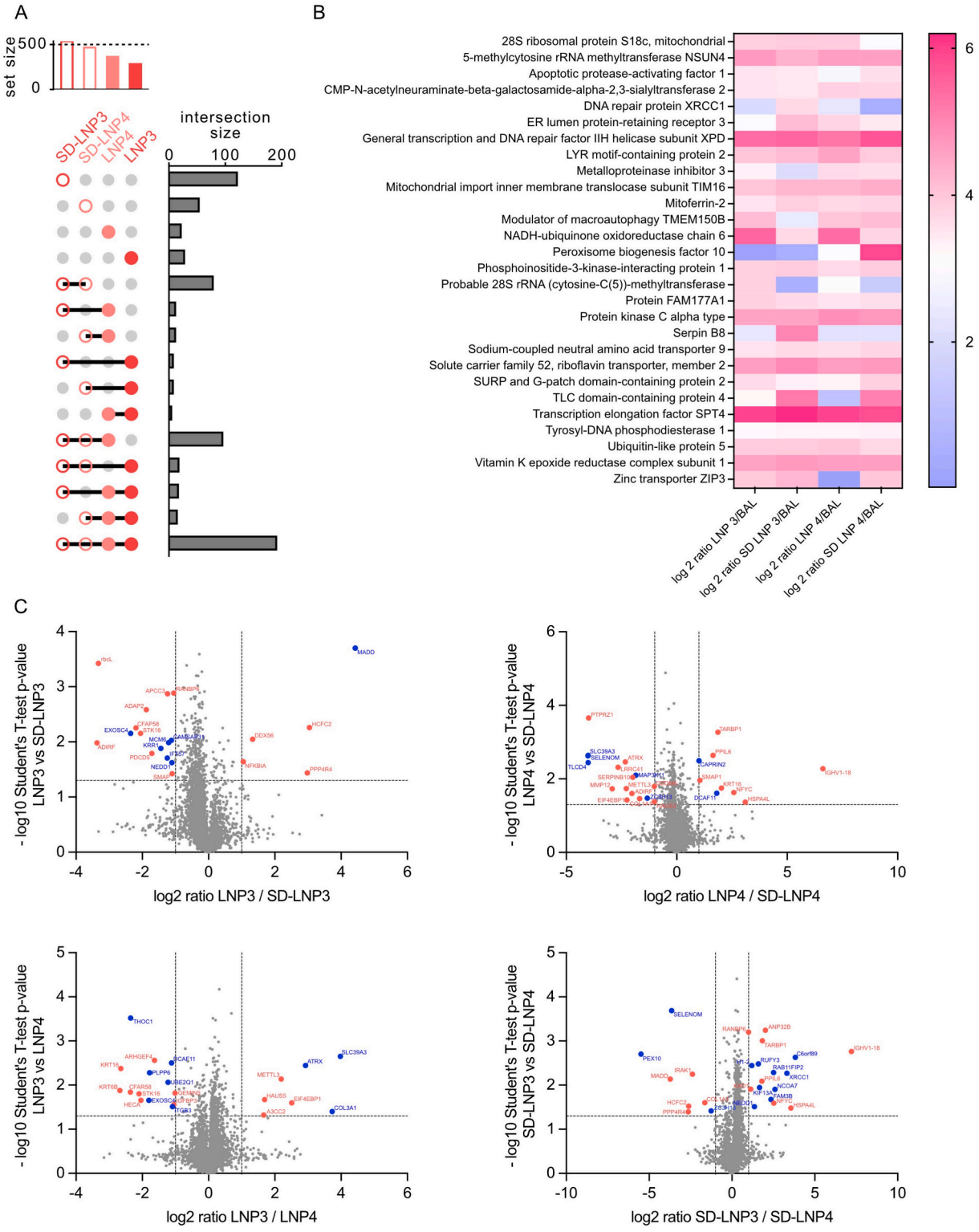

Fig. 6. Proteomic profiling of LNP protein coronas in human BALF. A) UpSet plot of log2 ratio of Samples/BALF >1. Set size indicates the number of proteins enriched 2-fold compared to BALF for each sample. A coloured dot indicates in which sample each intersection is found. Next to the intersections is a bar graph that shows the size of each intersection. If proteins are enriched in more than one sample, the dots are connected with a line. B) Heatmap showing log_2 enrichment ratios of the top 20 proteins per LNP formulation relative to BALF, highlighting distinct corona compositions. C) Volcano plots depicting differentially abundant proteins across LNP formulations. Red indicates proteins enriched more than two-fold in the corona relative to the compared formulation; blue marks proteins that are both significantly different and enriched compared to BALF. (For interpretation of the references to colour in this figure legend, the reader is referred to the web version of this article.)

inter-individual variability in corona formation; to maintain experimental consistency and focus on mechanistic aspects, BALF from a single donor was used in this study. Our findings help address the gap in understanding how inhalable LNPs interact with pulmonary fluids under clinically relevant conditions, which becomes increasingly relevant as clinical programs involving inhalable LNPs advance, e.g., ReCode Therapeutics' RCT2100, an inhaled mRNA–LNP candidate for cystic fibrosis that has entered Phase 1b (NCT06237335). These developments underscore the importance of pulmonary-specific profiling for inhaled LNPs. Future work involving larger donor cohorts, disease-relevant BALF samples, and comparisons across lung fluids and harvesting methods will be essential to define the principles governing corona formation in vivo and their implications for the rational design of pulmonary-administered LNPs.

4. Conclusion

SD induces persistent structural changes in LNPs that extend beyond size and encapsulation efficiency, reshaping membrane organization and downstream biological performance. Our data show that excipient–lipid interactions, particularly between PEG-lipid, helper lipids, and lactose, stabilize ordered membrane states that impair performance, especially in Onpattro-like formulations. These effects depend sensitively on LNP composition, underscoring the need for rational lipid selection, formulation tuning, and structural profiling tailored to the administration route. Traditional characterization tools fail to capture these changes, highlighting the value of orthogonal methods to monitor membrane alterations. Protein corona formation in human BAL fluid further amplifies formulation-specific differences, revealing new challenges and opportunities for pulmonary delivery. Collectively, our findings advocate for a shift in dry powder LNP design—from simple size-based optimization toward a multifactorial framework that integrates molecular interactions, membrane dynamics, and the complex biological microenvironment of the human lung.

Statement of ethics approval

Human bronchoalveolar lavage (BAL) fluid was obtained under the CPC-M bioArchive Steering Committee approved project BA-207/2025, titled "*Engineering protein and excipient interactions to unlock the potential of RNA-lipid nanoparticles in dry powder formulations for local pulmonary administration.*" The study was approved by the local ethics committee of the Ludwig-Maximilians University of Munich, Germany (Ethic vote #19–629). Written informed consent was obtained for all study participants.

Statement for the use of LLMs

During the preparation of this work the authors used ChatGPT to improve readability and language. The text was reviewed afterwards, and the authors take full responsibility for the content of the publication.

CRediT authorship contribution statement

Nora Martini: Writing – original draft, Visualization, Validation, Methodology, Formal analysis, Data curation, Conceptualization, Investigation. **Leonie Deßloch:** Writing – original draft, Visualization, Validation, Methodology, Investigation, Formal analysis, Data curation, Conceptualization. **Taras Sych:** Writing – original draft, Methodology, Investigation, Formal analysis, Data curation. **Otto Berninghausen:** Methodology, Investigation, Data curation. **J. Merl-Pham:** Methodology, Formal analysis, Data curation. **Sjoerd Dijkstra:** Methodology, Data curation. **Simone P. Carneiro:** Methodology, Data curation. **Marion Frankenberger:** Resources, Methodology. **Roland Beckmann:** Resources. **Jürgen Behr:** Resources, Methodology. **Gabriele Matschiner:** Validation, Supervision, Project administration, Investigation, Formal analysis, Conceptualization. **Christine Schuberth-Wagner:** Supervision, Investigation, Formal analysis, Conceptualization. **A. Önder Yildirim:** Supervision, Resources, Funding acquisition. **David C. Jürgens:** Writing – review & editing, Supervision, Methodology, Investigation, Data curation, Conceptualization. **Erdinc Sezgin:** Supervision, Resources, Methodology, Funding acquisition. **Olivia M. Merkel:** Writing – review & editing, Supervision, Funding acquisition. **Benjamin Winkeljann:** Writing – review & editing, Supervision, Resources, Project administration, Investigation, Funding acquisition, Conceptualization.

Declaration of competing interest

O.M. is a consultant for AbbVie Deutschland GmbH and for PARI Pharma GmbH. O.M. is an advisory board member for Coriolis Pharma GmbH and Corden Pharma GmbH, and for AMW GmbH on unrelated projects. L.D., C.S., D.J., O.M., and B.W., have equity interests in RNhale GmbH.

Acknowledgments

O.M. acknowledges funding from the DFG (Project 516634310) and the European Research Council (ERC-2022-COG-101088587). This work was supported through the Leibniz Supercomputing Centre in the framework of the project *AVOCADO2* to B.W. ES and TS have been supported by Swedish Research Council Grants (grant no. 2020-02682, 2024-02993 and 2024-00289), Wellcome Leap's Dynamic Resilience Program (jointly funded by Temasek Trust), Karolinska Institutet (2024-03250; 2024-03341; 2022-00803; 2020-00997), Cancer Research KI (2024-03488), Human Frontier Science Program (RGP0025/2022), Longevity Impetus Grant from Norn Group, Hevolution Foundation and Rosenkranz Foundation. We thank the SciLifeLab Advanced Light Microscopy facility and National Microscopy Infrastructure (VR-RFI 2016-00968) for their support on imaging. We gratefully acknowledge the provision of human biomaterial (BAL fluid samples) and clinical data from the CPC-M bioArchive and its partners at the Asklepios Biobank Gauting, the LMU Hospital and the Ludwig-Maximilians-Universität München. We thank the patients and their families for their support. Figures include graphical elements created using BioRender (license held by BW).

Appendix A. Supplementary data

Supplementary data to this article can be found online at https://doi.org/10.1016/j.jconrel.2025.114539.

Data availability

Data will be made available on request.

References

[1] Lives saved by COVID-19 vaccines, J. Paediatr. Child Health 58 (2022), https://doi.org/10.1111/jpc.16213, 2129-2129.
[2] K.S. Arte, et al., Recent advances in drying and development of solid formulations for stable mRNA and siRNA lipid nanoparticles, J. Pharm. Sci. 114 (2025) 805–815.
[3] C.M. Zimmermann, et al., Spray drying siRNA-lipid nanoparticles for dry powder pulmonary delivery, J. Control. Release 351 (2022) 137–150.
[4] K.P. Friis, et al., Spray dried lipid nanoparticle formulations enable intratracheal delivery of mRNA, J. Control. Release 363 (2023) 389–401.
[5] A. Gordon, B. Li, J. Witten, H. Nguyen, D.G. Anderson, Inhalable dry powders for lung mRNA delivery, Adv. Healthc. Mater. 13 (2024) 2400509.
[6] H. Takahashi, A. Matsuo, I. Hatta, Effects of salt on the lamellar and bicontinuous cubic phases of fully hydrated monoacylglycerol (monoelaidin), Phys. Chem. Chem. Phys. 4 (2002) 2365–2370.
[7] A.S. Rudolph, B. Goins, The effect of hydration stress solutes on the phase behavior of hydrated dipalmitoylphosphatidylcholine, Biochim. Biophys. Acta 1066 (1991) 90–94.

[8] G. Cevc, Effect of lipid headgroups and (nonelectrolyte) solution on the structural and phase properties of bilayer membranes, Ber. Bunsen. Phys. Chem 92 (1988) 953A–961.
[9] B. Demé, T. Zemb, Measurement of sugar depletion from uncharged lamellar phases by SANS contrast variation, J. Appl. Cryst. 33 (2000) 569–573.
[10] T. Söderlund, J.-M.I. Alakoskela, A.L. Pakkanen, P.K.J. Kinnunen, Comparison of the effects of surface tension and osmotic pressure on the interfacial hydration of a fluid phospholipid bilayer, Biophys. J. 85 (2003) 2333–2341.
[11] J. Stümpel, W.L.C. Vaz, D. Hallmann, An X-ray diffraction and differential scanning calorimetric study on the effect of sucrose on the properties of phosphatidylcholine bilayers, Biochim. Biophys. Actavv 821 (1985) 165–168.
[12] S. Leekumjorn, A.K. Sum, Molecular investigation of the interactions of trehalose with lipid bilayers of DPPC, DPPE and their mixture, Mol. Simul. 32 (2006) 219–230.
[13] A. Skibinsky, R.M. Venable, R.W. Pastor, A molecular dynamics study of the response of lipid bilayers and monolayers to trehalose, Biophys. J. 89 (2005) 4111–4121.
[14] M.A. Villarreal, S.B. Díaz, E.A. Disalvo, G.G. Montich, Molecular dynamics simulation study of the interaction of trehalose with lipid membranes, Langmuir 20 (2004) 7844–7851.
[15] J.H. Crowe, M.A. Whittam, D. Chapman, L.M. Crowe, Interactions of phospholipid monolayers with carbohydrates, Biochim. Biophys. Acta 769 (1984) 151–159.
[16] F. Lairion, E.A. Disalvo, Effect of trehalose on the contributions to the dipole potential of lipid monolayers, Chem. Phys. Lipids 150 (2007) 117–124.
[17] C. Lambruschini, A. Relini, A. Ridi, L. Cordone, A. Gliozzi, Trehalose interacts with phospholipid polar heads in Langmuir monolayers, Langmuir 16 (2000) 5467–5470.
[18] M. del C. Luzardo, et al., Effect of trehalose and sucrose on the hydration and dipole potential of lipid bilayers, Biophys. J. 78 (2000) 2452–2458.
[19] G. Strauss, P. Schurtenberger, H. Hauser, The interaction of saccharides with lipid bilayer vesicles: stabilization during freeze-thawing and freeze-drying, Biochim. Biophys. Acta 858 (1986) 169–180.
[20] T. Parasassi, E.K. Krasnowska, L. Bagatolli, E. Gratton, Laurdan and Prodan as Polarity-sensitive Fluorescent Membrane Probes, 1998.
[21] H. Bekker, et al., Gromacs-A Parallel Computer for Molecular-dynamics Simulations, World Scientific Publishing, 1993, pp. 252–256.
[22] D. Van Der Spoel, et al., GROMACS: fast, flexible, and free, J. Comput. Chem. 26 (2005) 1701–1718.
[23] S. Pronk, et al., GROMACS 4.5: a high-throughput and highly parallel open source molecular simulation toolkit, Bioinformatics 29 (2013) 845–854.
[24] J. Lee, et al., CHARMM-GUI input generator for NAMD, GROMACS, AMBER, OpenMM, and CHARMM/OpenMM simulations using the CHARMM36 additive force field, J. Chem. Theory Comput. 12 (2016) 405–413.
[25] S. Jo, T. Kim, V.G. Iyer, W. Im, CHARMM-GUI: a web-based graphical user interface for CHARMM, J. Comput. Chem. 29 (2008) 1859–1865.
[26] E.L. Wu, et al., CHARMM-GUI membrane builder toward realistic biological membrane simulations, J. Comput. Chem. 35 (2014) 1997–2004.
[27] S. Feng, S. Park, Y.K. Choi, W. Im, CHARMM-GUI membrane builder : past, current, and future developments and applications, J. Chem. Theory Comput. 19 (2023) 2161–2185.
[28] S. Park, Y.K. Choi, S. Kim, J. Lee, W. Im, CHARMM-GUI membrane builder for lipid nanoparticles with Ionizable cationic lipids and PEGylated lipids, J. Chem. Inf. Model. 61 (2021) 5192–5202.
[29] J. Huang, A.D. MacKerell Jr., CHARMM36 all-atom additive protein force field: validation based on comparison to NMR data, J. Comput. Chem. 34 (2013) 2135–2145.
[30] S. Sabnis, et al., A novel amino lipid series for mRNA delivery: improved endosomal escape and sustained pharmacology and safety in non-human primates, Mol. Ther. 26 (2018) 1509–1519.
[31] G. Conte, et al., Hybrid lipid/polymer nanoparticles to tackle the cystic fibrosis mucus barrier in siRNA delivery to the lungs: does PEGylation make the difference? ACS Appl. Mater. Interfaces 14 (2022) 7565–7578.
[32] T. Sych, et al., High-throughput measurement of the content and properties of nano-sized bioparticles with single-particle profiler, Nat. Biotechnol. 42 (2024) 587–590.
[33] G.W. Hunninghake, J.E. Gadek, O. Kawanami, V.J. Ferrans, R.G. Crystal, Inflammatory and immune processes in the human lung in health and disease: evaluation by bronchoalveolar lavage, Am. J. Pathol. 97 (1979) 149–206.
[34] S.A. Dilliard, et al., The interplay of quaternary ammonium lipid structure and protein corona on lung-specific mRNA delivery by selective organ targeting (SORT) nanoparticles, J. Control. Release 361 (2023) 361–372.
[35] G. Porat-Dahlerbruch, et al., Spatial organization of lipid nanoparticle siRNA delivery systems revealed by an integrated magnetic resonance approach, Small Methods (2024) 2400622, https://doi.org/10.1002/smtd.202400622.
[36] L.I. Viera, S. Alonso-Romanowski, V. Borovyagin, M.R. Feliz, E.A. Disalvo, Properties of gel phase lipid-trehalose bilayers upon rehydration, Biochim. Biophys. Acta 1145 (1993) 157–167.
[37] H.D. Andersen, C. Wang, L. Arleth, G.H. Peters, P. Westh, Reconciliation of opposing views on membrane–sugar interactions, Proc. Natl. Acad. Sci. U. S. A. 108 (2011) 1874–1878.
[38] J. Kapla, et al., Molecular dynamics simulations of membrane–sugar interactions, J. Phys. Chem. B 117 (2013) 6667–6673.
[39] G. Moiset, et al., Disaccharides impact the lateral organization of lipid membranes, J. Am. Chem. Soc. 136 (2014) 16167–16175.
[40] S.S. Stachura, C.J. Malajczuk, R.L. Mancera, Does sucrose change its mechanism of stabilization of lipid bilayers during desiccation? Influences of hydration and concentration, Langmuir 35 (2019) 15389–15400.
[41] X. You, E. Lee, C. Xu, C.R. Baiz, Molecular mechanism of cell membrane protection by sugars: a study of interfacial H-bond networks, J. Phys. Chem. Lett. 12 (2021) 9602–9607.
[42] M. Li, et al., Lyophilization process optimization and molecular dynamics simulation of mRNA-LNPs for SARS-CoV-2 vaccine, npj Vaccin. 8 (2023) 153.
[43] J.A. Kulkarni, et al., On the formation and morphology of lipid nanoparticles containing ionizable cationic lipids and siRNA, ACS Nano 12 (2018) 4787–4795.
[44] J. Viger-Gravel, et al., Structure of lipid nanoparticles containing siRNA or mRNA by dynamic nuclear polarization-enhanced NMR spectroscopy, J. Phys. Chem. B 122 (2018) 2073–2081.
[45] M.F.W. Trollmann, R.A. Böckmann, Mechanistic Insight into pH-driven Phase Transition of Lipid Nanoparticles, 2024.11.27.625717 Preprint at doi:, 2024 https://doi.org/10.1101/2024.11.27.625717.
[46] E.A. Golovina, A.V. Golovin, F.A. Hoekstra, R. Faller, Water replacement hypothesis in atomic detail—factors determining the structure of dehydrated bilayer stacks, Biophys. J. 97 (2009) 490–499.
[47] M.M. Wang, et al., Elucidation of lipid nanoparticle surface structure in mRNA vaccines, Sci. Rep. 13 (2023) 16744.
[48] C. Hald Albertsen, et al., The role of lipid components in lipid nanoparticles for vaccines and gene therapy, Adv. Drug Deliv. Rev. 188 (2022) 114416.
[49] H. Orlikowska-Rzeznik, E. Krok, M. Chattopadhyay, A. Lester, L. Piatkowski, Laurdan discerns lipid membrane hydration and cholesterol content, J. Phys. Chem. B 127 (2023) 3382–3391.
[50] B. Kent, et al., Measurement of glucose exclusion from the fully hydrated DOPE inverse hexagonal phase, Soft Matter 6 (2010) 1197.
[51] K.B. Konov, et al., Membrane–sugar interactions probed by pulsed electron paramagnetic resonance of spin labels, J. Phys. Chem. B 119 (2015) 10261–10266.
[52] C.S. Pereira, P.H. Hünenberger, Effect of trehalose on a phospholipid membrane under mechanical stress, Biophys. J. 95 (2008) 3525–3534.
[53] A. Roy, R. Dutta, N. Kundu, D. Banik, N. Sarkar, A comparative study of the influence of sugars sucrose, trehalose, and maltose on the hydration and diffusion of dmpc lipid bilayer at complete hydration: investigation of structural and spectroscopic aspect of lipid–sugar interaction, Langmuir 32 (2016) 5124–5134.
[54] Y. Mo, et al., Lipid-siRNA organization modulates the intracellular dynamics of lipid nanoparticles, J. Am. Chem. Soc. (2025), https://doi.org/10.1021/jacs.4c18308 jacs.4c18308.
[55] S. Meulewaeter, et al., Continuous freeze-drying of messenger RNA lipid nanoparticles enables storage at higher temperatures, J. Control. Release 357 (2023) 149–160.
[56] G. Sahay, D.Y. Alakhova, A.V. Kabanov, Endocytosis of nanomedicines, J. Control. Release 145 (2010) 182–195.
[57] J.J. Rennick, A.P.R. Johnston, R.G. Parton, Key principles and methods for studying the endocytosis of biological and nanoparticle therapeutics, Nat. Nanotechnol. 16 (2021) 266–276.
[58] Y. Sakurai, et al., siRNA delivery to lymphatic endothelial cells via ApoE-mediated uptake by lipid nanoparticles, J. Control. Release 353 (2023) 125–133.
[59] K. Liu, et al., Multiomics analysis of naturally efficacious lipid nanoparticle coronas reveals high-density lipoprotein is necessary for their function, Nat. Commun. 14 (2023) 4007.
[60] L. Miao, et al., Synergistic lipid compositions for albumin receptor mediated delivery of mRNA to the liver, Nat. Commun. 11 (2020) 2424.
[61] A. Gallud, et al., Time Evolution of PEG-shedding and Serum Protein Coronation Determines the Cell Uptake Kinetics and Delivery of Lipid Nanoparticle Formulated mRNA, Preprint at, 2021, https://doi.org/10.1101/2021.08.20.457104.
[62] J. Gilleron, et al., Image-based analysis of lipid nanoparticle–mediated siRNA delivery, intracellular trafficking and endosomal escape, Nat. Biotechnol. 31 (2013) 638–646.
[63] J. Liu, Y.-Y. Liu, C.-S. Li, A. Cao, H. Wang, Exocytosis of nanoparticles: a comprehensive review, Nanomaterials 13 (2023) 2215.
[64] L. Hagedorn, D.C. Jürgens, O.M. Merkel, B. Winkeljann, Endosomal escape mechanisms of extracellular vesicle-based drug carriers: lessons for lipid nanoparticle design, in: Extracell Vesicles Circ Nucleic Acids 5, 2024, pp. 344–357.
[65] A. Wittrup, et al., Visualizing lipid-formulated siRNA release from endosomes and target gene knockdown, Nat. Biotechnol. 33 (2015) 870–876.
[66] N. Aliakbarinodehi, et al., Time-resolved inspection of ionizable lipid-facilitated lipid nanoparticle disintegration and cargo release at an early endosomal membrane mimic, ACS Nano 18 (2024) 22989–23000.
[67] K.H. Kim, et al., Biophysical characterization of siRNA-loaded lipid nanoparticles with different PEG content in an aqueous system, Eur. J. Pharm. Biopharm. 190 (2023) 150–160.
[68] B. Button, et al., A Periciliary brush promotes the lung health by separating the mucus layer from airway epithelia, Science 337 (2012) 937–941.
[69] J.V. Fahy, B.F. Dickey, Airway mucus function and dysfunction, N. Engl. J. Med. 363 (2010) 2233–2247.
[70] B. Tafech, et al., Exploring mechanisms of lipid nanoparticle-mucus interactions in healthy and cystic fibrosis conditions, Adv. Healthc. Mater. 13 (2024) 2304525.
[71] Physiology and Pathophysiology of Human Airway Mucus, 2022. https://journals.physiology.org/doi/epdf/10.1152/physrev.00004.2021. https://doi.org/10.1152/physrev.00004.2021.
[72] S. Magramane, Z. Pápay, B. Turbucz, I. Antal, Formulation and characterization of pulmonary drug delivery systems, Acta Pharm. Hung. 89 (2019) 63–83.
[73] S.K. Lai, Y.-Y. Wang, D. Wirtz, J. Hanes, Micro- and macrorheology of mucus, Adv. Drug Deliv. Rev. 61 (2009) 86–100.

[74] B.S. Schuster, J.S. Suk, G.F. Woodworth, J. Hanes, Nanoparticle diffusion in respiratory mucus from humans without lung disease, Biomaterials 34 (2013) 3439–3446.
[75] H.M. Braakhuis, et al., An air-liquid interface bronchial epithelial model for realistic, repeated inhalation exposure to airborne particles for toxicity testing, JoVE (2020) 61210, https://doi.org/10.3791/61210.
[76] D. Sanchez-Guzman, et al., Long-term evolution of the epithelial cell secretome in preclinical 3D models of the human bronchial epithelium, Sci. Rep. 11 (2021) 6621.
[77] Q. Cheng, et al., Selective organ targeting (SORT) nanoparticles for tissue-specific mRNA delivery and CRISPR–Cas gene editing, Nat. Nanotechnol. 15 (2020) 313–320.
[78] D.O. Weise, et al., An optimized workflow for MS-based quantitative proteomics of challenging clinical bronchoalveolar lavage fluid (BALF) samples, Clin. Proteomics 20 (2023) 14.
[79] A. Lex, N. Gehlenborg, H. Strobelt, R. Vuillemot, H. Pfister, UpSet: visualization of intersecting sets, IEEE Trans. Vis. Comput. Graph. 20 (2014) 1983–1992.
[80] M.J. Hajipour, et al., An overview of nanoparticle protein corona literature, Small 19 (2023) 2301838.
[81] S. Rademacker, et al., The impact of lipid compositions on siRNA and mRNA lipid nanoparticle performance for pulmonary delivery, Eur. J. Pharm. Sci. 212 (2025) 107182.